UNIVERSITY OF BIRMINGHAM

QUANTUM SIMULATIONS WITH ULTRA-COLD ATOMS

by

SYMRAN WEDGE

A thesis submitted to the University of Birmingham for the degree of

MASTER OF RESEARCH

Cold Atoms

School of Physics and Astronomy

Supervisor: Prof. Giovanni Barontini

University of Birmingham

March 2024

Abstract

This experiment has focused on using optical potentials produced by a digital micro-mirror device (DMD) to simulate Fermi-Acceleration on ultra-cold atoms. Fermi Acceleration is a mechanism which explains how high energy cosmic rays gain non-thermal energies and is of importance in astrophysical events such as supernovas. In the experiment, ultra cold atoms are produced in an elongated 3D harmonic trap to create a thermal cloud. The cloud of atoms are loaded in a optical lattice potential which drives the cloud towards a barrier, where the atoms get reflected. This is analogous to Fermi-Acceleration where particles interact with shock waves in different astrophysical environments. In this report it is observed how the effect of changing the driving frequency (ω), wavenumber (ϕ), amplitude (A) and trapping frequency of the potential on both the optical lattice velocity (v_i) and reflection velocity (v_r) of the cloud of atoms. The experimental results effectively demonstrates that the cold atom set-up is a valid analogy of Fermi-Acceleration since the results display that the optical lattice velocity as well as the reflection velocity follow the theoretical predictions across the parameter changes in the specific regimes. This study has shown that a cold atom set-up can be used as an effective way of modelling Fermi-Acceleration experimentally. It highlights the importance of cold atom experiments for studying wider physics phenomena and, in the case of Fermi-Acceleration, experimental verification of the Bell's Power Law distribution has never been carried out experimentally to date. The validity for cold atom experiments to model this effect means the law can now be experimentally verified.

Contents

List of Figures

List of Tables

Chapter 1

Introduction

Ultra-cold atomic Physics is a branch of condensed matter Physics that utilises atoms with temperatures nearing absolute zero. This is beneficial as at low temperatures the quantum mechanical properties of an atom become extremely important and can be manipulated experimentally. The creation of the first optical dipole trap in 1986 [1] was followed by the first magneto-optical trap in 1987 [2] and provided momentum to the cold atom field since there were finally methods available to trap and manipulate atoms while simultaneously cooling them to temperatures near absolute zero. Over the years, laser cooling techniques have been further developed, resulting in trap systems for single atoms [3] and molecules [4]. These developments have led to a much wider range of experimentation possible, advancing knowledge in many areas, such as ultra-cold chemistry [5], quantum magnetism [6] and bosonic superfluidity [7] to name a few. One of the most important discoveries is the observation of the Bose-Einstein Condensate (BEC).

1.1 Overview

The report will be structured as follows: it will begin with a short introduction about Bose-Einstein Condensates, highlighting what they are and how they are formed. The next section will describe the experimental set-up, including a discussion of the vacuum, laser and locking systems and how they are used to cool down atoms. This will lead into a discussion of how optical potentials are generated in the experiment and how they are used to manipulate and run experiments on the ultra-cold atoms.

In the final parts of the report the work carried out into the investigation of Fermi Acceleration using the cold atoms produced in the experiment along with the digital micro-mirror device (DMD), will be detailed. The report will finish with a look into how the work on Fermi Acceleration can be extended.

1.2 Bose-Einstein Condensation

Bose-Einstein Condensation is a quantum effect observed when a low-density gas of bosons is cooled down to temperatures close to absolute zero, resulting in a large fraction of the bosons occupying the lowest energy state available. The theory for the effect was first developed by Bose in 1924 [8] and then developed by Einstein [9] in the same year. It was first observed in 1995 from a series of experiments using Rubidium [10] and then Sodium [11] vapours. The signatures of the BEC were observed as a sharp peak in the velocity distribution of the alkali atoms under certain critical temperatures. Figure 1.1 is an image of the first atomic cloud of Rubidium. As well as this, in the same year, the first signatures of BEC formation in Lithium vapours was observed [12]. These early observations helped build a foundation for the field of ultra-cold atoms. BECs are an integral part of ultra-cold atomic gas experiments since they are very good quantum simulators, [13] and can be used to model a variety of quantum effects, such as the fountain effect which will be discussed later in the report. They also have practical uses and have been used in atomic clocks [14, 15], magnetic sensors [16, 17], temperature sensors [18] and can be used in atom interferometers [19, 20, 21, 22], which are devices that can be used to calculate measurements of acceleration and gravity [23, 24].

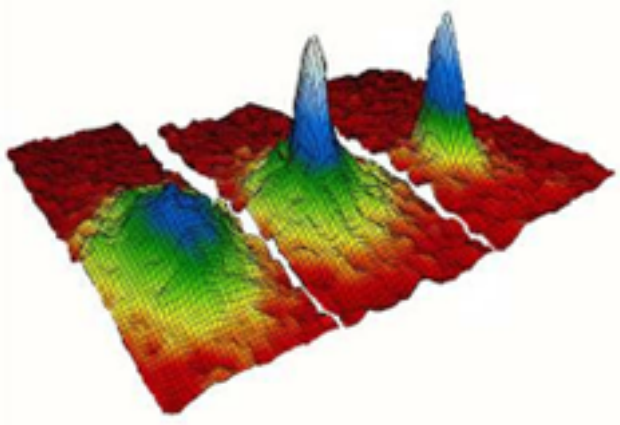

Figure 1.1: Image of the velocity distribution of Rubidium atoms taken from [10]. The colours correspond to the number of atoms at each velocity with white being the greatest number of atoms and red being the fewest number of atoms. The left most image shows the gas at a temperature above condensation; the middle image shows the atoms just after the formation of the condensate; and the right image is the atoms at nearly a pure condensate.

Only bosonic matter can form a Bose Einstein Condensate. Figure 1.2 is a diagram representing the energy levels in a Boson vs a Fermion. Each line represents an energy level which increases as you go up. The diagram shows that unlike in Fermions, an unlimited number of identical bosons can occupy the same energy levels. The Pauli Exclusion principle states that identical particles with half integer spins cannot occupy the same quantum state simultaneously (i.e. have the same quantum numbers). Fermions have half-integer spin, and thus cannot occupy the same level. Unlike fermions, bosons have integer spins therefore this principle does not apply to them. The probability amplitude is given by

$$\Psi = \Psi_1(a)\Psi_2(b) \pm \Psi_1(b)\Psi_2(a), \tag{1.1}$$

where “a” and “b” are both states that electrons (or a particle) can occupy.

Fermions, which have half-integer spin have antisymmetric wavefunctions (minus sign is applied), while bosons, which have integer spin, have symmetric wavefunctions (plus sign is applied). Eq. 1.1 therefore shows one of the main outcomes of the Pauli exclusion principle. If both fermions 1 and 2 are in state "a" (or "b"), then the wavefunction will be zero - this is not a possible state. Meanwhile, if both bosons 1 and 2 are in state "a" (or "b"), the wavefunction is non zero, meaning this is possible.

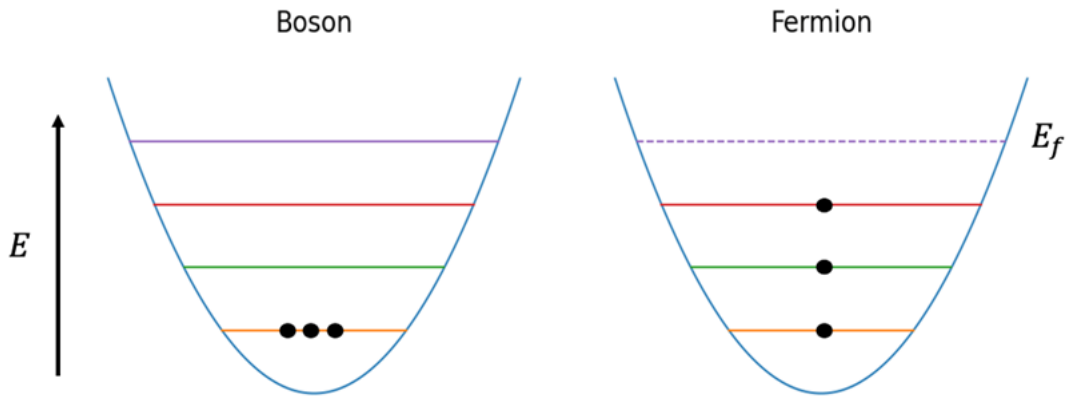

Figure 1.2: Image of Boson vs Fermion energy diagram representing energy levels and the Pauli Exclusion principle.

When a BEC forms, the atoms occupy (usually) the ground state energy level. When the number of atoms occupying the ground state becomes on the same order as the total number of atoms in the cloud, the cloud can be described as BEC.

The following equations have been taken from a paper written by F. Dalfovo, [25]. In order for a BEC to form, the phase space density, P_{sd}, must be much greater than one, given by

$$P_{sd} = \rho\lambda_B^3 >> 1, \tag{1.2}$$

where ρ is the number density (of atoms) and λ_B is de Broglie wavelength (thermal).

This can be achieved experimentally by reducing the temperature, which in turn increases λ_B, demonstrated by

$$\lambda_B = \frac{h}{\sqrt{3mk_BT}}, \tag{1.3}$$

where m is the mass of the atom, T is the temperature of the cloud and k_B is the Boltzmann constant.

Bose-Einstein Condensation is also limited by temperature. Formation can only happen below critical temperature, which is described by

$$T_c = \frac{\hbar\omega_{h0}}{k_B}\left(\frac{N}{\zeta(3)}\right)^{\frac{1}{3}}, \tag{1.4}$$

where ω_{ho} is the geometric average of the trapping frequencies, N is the number of atoms and ζ(n)= Riemann Zeta Function.

Since it is not experimentally possible to reach absolute zero, there will always be a small number of atoms that remain thermally distributed within the condensed cloud, which results in a bimodal distribution (double peaks) of the cloud in both real and momentum space. The condensed part of the cloud appears as a sharp peak at the centre of the cloud, which can be seen in Figure 1.3. When the blue line gets thinner and sharper the cloud is more condensed and a BEC is formed. Whereas when the blue line is wider and flatter, the cloud is more thermal. We can measure how condensed the cloud is using the condensate fraction, which is described by

$$\frac{N_0}{N} = 1 - \left(\frac{T}{T_c}\right)^3. \tag{1.5}$$

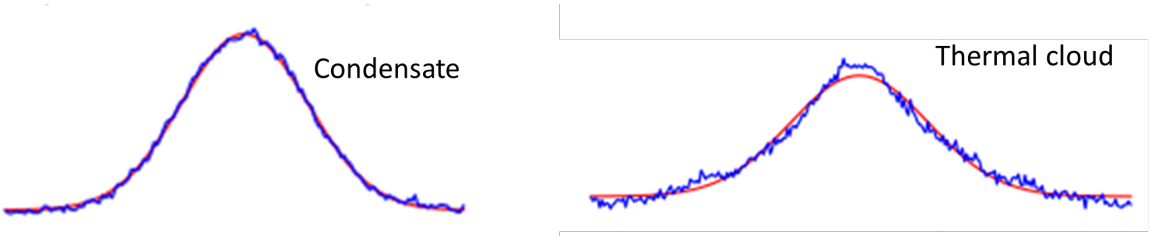

Figure 1.3: Images of the distribution for condensed and thermal clouds. The blue line is sharper and thinner when the cloud is a condensate, whereas it becomes wider when it is a thermal cloud. This is an image taken from the experiment.

Another important parameter of the condensate that can be calculated is the Thomas-Fermi (TF) radius which is derived from the Gross-Pitaeveskii equation and holds true as long the Thomas-Fermi approximation is valid. The TF radius is given by

$$R = \sqrt{\frac{2\mu}{m\omega_{ho}^2}}, \tag{1.6}$$

where μ is the chemical potential, m is the mass of the atom and ω_{ho} is the trapping frequency.

The TF approximation assumes that the effect of kinetic energy is negligible, because all interactions within the cloud are highly repulsive, due to the harmonic potential the cloud is trapped in. In the TF approximation, the density of the atom cloud is the same shape as the potential of the cloud. The chemical potential is defined as

$$\mu = \frac{\hbar\omega_{ho}}{2}\left(\frac{15Na}{a_{ho}}\right)^{2/5}, \tag{1.7}$$

where N is the number of atoms, a is the scattering length, a_{ho} is the harmonic oscillator length, given by $\sqrt{\frac{\hbar}{m\omega_{ho}}}$. The size of the cloud is independent of the number of atoms and is determined by a_{ho}, which corresponds to the average Gaussian width and is fixed by the trapping frequencies of the cloud, ω_{ho}. The chemical potential is greater than the potential of the cloud in the condensate and zero elsewhere.

The TF radius is the radius at the point where the density should go to zero. As long as the TF approximation holds, the TF radius can be thought of as the radius of the condensate. In an asymmetric harmonic trap or for where the BEC shape is elliptical, there is a TF radius in the three axial directions, r_x, r_y and r_z. The TF radius is an important parameter to know as it can be useful for finding the critical frequency needed to create a vortex, [26].

In a cloud of atoms, the atoms experience forces from both quantum pressure and the interaction of the bosons with each other. The balance between the quantum pressure and the interaction energy occurs at the healing length, given by

$$\xi = \sqrt{\frac{1}{8\pi na}}. \tag{1.8}$$

The healing length refers to the minimum distance over which the order parameter can heal. In terms of the BEC, the healing length describes how quickly the wave function adjusts when changes in the potential are made. Healing length is an important parameter in superfluid effects. For example, it can be used to estimate the size of vortices that form in superfluids, [27].

1.3 Gross-Pitaeveskii equation

Since bosons in a BEC are all in the same quantum state, they can be described by the same wave-function. The ground state equation for identical bosons occupying the same state is known as the Gross–Pitaevskii equation [28, 29]. The time independent form of the GPE is given by

$$\mu\Psi(\mathbf{r}) = (-\frac{h}{2m}\nabla^2 + V(\mathbf{r}) + g|\Psi(\mathbf{r})|^2)\Psi(\mathbf{r}), \tag{1.9}$$

where

$g = \frac{4\pi\hbar^2 a}{m}$,

V = Potential (e.g harmonic trap),

Ψ = Wavefunction,

μ = Chemical Potential, and

m = Mass of the Bosonic matter.

The equation has the same form as the Schrodinger equation with the addition of an interaction term which has a coupling constant, g which is proportional to the s- wave scattering length, a. Setting the coupling constant to zero recovers the single particle Schrodinger equation. The GPE is important since it can be used to obtain information about a BEC in potentials and harmonic traps, which can be extremely important for choosing and calculating parameters for experiments. For example, solving the GPE can give insight into the spatial distribution of a condensates density within a trap. This information is important for understanding the shape and size of the BEC under different trapping frequencies. Since the GPE is a partial differential equation, it can be used to describe the time evolution of the wave function for the BEC. This can be done by numerically solving the equation.

1.4 Dynamic Optical Potentials

Dynamic optical potentials are key tools used in ultra-cold atom experiments [30, 31, 32]. When an optical potential is applied to a cloud of atoms, the atoms experience an A.C Stark shift and feel a potential which is proportional to the intensity of an off-resonant light field. The A.C Stark effect is the effect of splitting of a spectral line into several components in the presence of a time varying electric field. In this experiment, the atoms are pre-cooled and trapped in a magneto-optical trap. The atoms are then loaded into a crossed optical dipole trap to be cooled further by evaporative cooling and are held in a near harmonic trap where they are manipulated by optical potentials using a specially shaped beam. The optical dipole trap will be discussed later on in the report, but first I will give a brief introduction behind the theory of optical potentials since they are fundamental to understanding the experiment.

Optical dipole potentials have two main components: the interaction dipole potential, U_{dip}, and the scattering potential, γ_{scatt}. A more detailed overview of optical potentials is given in [33] and a short summary of the results will be given below.

Consider a neutral atom oscillating in an electric field, $\mathbf{E}$. The atom has an induced dipole moment related to the field amplitude, p given by

$$\mathbf{p} = \alpha \mathbf{E}, \tag{1.10}$$

where α depends on the driving frequency, ω, and is known as the complex polarizability.
This results in interaction dipole potential of the induced dipole moment U_{dip}, which is given by

$$U_{dip} = \frac{1}{2} < \mathbf{pE} >= \frac{Re(\alpha)I}{2\epsilon_0 c}, \tag{1.11}$$

where I is the intensity of the light, given by $2\epsilon_0 c|\mathbf{E}|^2$, and <**pE**> denotes the time average. The factor of a half is because the dipole moment is induced rather than permanent.

Consider the laser light that interacts with the atoms as a stream of a photons, $\hbar\omega$. The scattering rate,

Γ_{scatt}, is given by

$$\Gamma_{scatt} = \frac{P_{abs}}{\hbar\omega} = \frac{Im(\alpha)I}{\hbar\epsilon_0 c}, \tag{1.12}$$

where P_{abs} is the power absorbed by the oscillator from the driving field.

It can be thought of in terms of photon emission and re-emission cycles during the spontaneous emission that occurs after a photon has been absorbed by an atom.

Eq. 1.11 and Eq. 1.12 express the two main areas of interest for dipole traps. These equations can be used to calculate the potential for a given beam power and expected heating rate for the trap. More details on how these equations are used in experimental systems can be found in [33].

In practice, the atoms must be considered as multilevel atoms. In this case, the potential is treated as a perturbation to the ground state energy, so the equations for the potential and scattering rate become those given by

$$U_{dip} = \frac{c^2\pi\Gamma}{2\omega_0^3}\left(\frac{2 + P_{g_f m_f}}{\triangle_{2,F}} + \frac{1 - P_{g_f m_f}}{\triangle_{1,F}}\right)I(r) \tag{1.13}$$

and

$$\Gamma_{scatt} = \frac{c^2\pi\Gamma^2}{2\hbar\omega_0^3}\left(\frac{2}{\triangle_{2,F}^2} + \frac{1}{\triangle_{1,F}^2}\right)I(r) \tag{1.14}$$

respectively, where Γ is the damping rate, which corresponds to the spontaneous decay rate of the excited atomic level, P characterises the polarisation of the laser, $\triangle_{1,F}$ and $\triangle_{2,F}$ are frequency detunings of the laser. The detuning of the D1 and D2 transition line in Rubidium-87 must be considered separately, and are denoted by the $\triangle_{1,F}$ and $\triangle_{1,F}$ terms respectively. P = 0 or ± 1 for linearly or circularly polarised light respectively.

Optical dipole potentials can be attractive or repulsive. An attractive potential occurs when the frequency of the light is below an atomic resonance, called red detuning where $\triangle$<0. The dipole potential for an attractive potential is negative and hence an atom is attracted to the intensity maxima of the light field. Attractive potentials can be utilised to trap atoms in optical tweezers [34, 35, 36]. Attractive potentials are also used to focus cold atom cloud at the centre of a dipole trap [37] which is what happens in this experiment. Repulsive optical potentials can be implemented in cold atoms experiments also [38, 39] and occur above atomic resonance, when the light is blue detuned, and $\triangle$>0.

When atoms interact with the repulsive potential the dipole interaction repels them out of field and a potential minimum corresponds to minima of the intensity. For attractive potentials, potential minima are found at positions of maximum intensity.

Dipole traps usually have a large detuning along with high intensities in order to keep the scattering rates as low as possible. This is because dipole potential scales as $\frac{1}{\triangle}$whereas scattering rate scales as $\frac{1}{\triangle^2}$. In the experiment, the cross-dipole trap and the DMD use optical potentials to trap and manipulate the atoms respectively.

Chapter 2

Experimental set-up

In this section the experimental setup will be discussed. Firstly a brief overview of the experiment will be given, followed by an in depth explanation of the laser systems used in the experiment and how the DMD is used to generate optical potentials. Finally, the control system which manipulates the atom cloud and laser system will be described. The experiment was originally built in 2017 and a detailed description of the original setup can be found in [40].

In 2022, a new imprinting laser was introduced to the experimental setup as part of the introductory work for this thesis. Aside from this addition, no other components were modified. However, the experimental configuration was adjusted to accommodate the new experiment investigated in this work. This involved realigning the laser, optics, and mirrors to alter the trapping frequency, as discussed in detail later. Additionally, the optical path was realigned daily as the setup is sensitive to small vibrations and temperature fluctuations. Each morning, the atom number and temperature were checked to ensure the formation of a condensate. If the atom cloud was too hot or the atom number too low after alignment, the laser positions and the cross of the dipole trap was calibrated, which is discussed further below.

Figure 2.1 is an image of the experimental apparatus with some of the key components labeled. Specific laser setups will be discussed and shown in more detail later on in this section.

2.1 Brief overview

In the experiment, the species used to form a BEC is Rubidium-87. An ^{87}Rb atom contains 37 protons and electrons, and 50 neutrons, so is a composite boson, meaning multiple atoms can occupy the same energy state. ^{87}Rb is the preferable species for making a BEC since it has a positive scattering length which means it is repulsive at low temperatures - preventing the collapse of all but the smallest of condensates, [41]. For the ^{87}Rb atoms to form a BEC the atoms must be cooled down to extremely low temperatures close to absolute zero. Initially this is done through laser cooling in the 2D and 3D magneto-optical traps, labeled in figure 2.1. The atoms are then transferred to an optical dipole trap, where they are cooled further by evaporative cooling.

The most important feature of the physical apparatus is the integration of a digital micro-mirror device (DMD) in the system, which allows for direct interaction with the BEC through dynamic optical potentials, as well as the microscope objective that is used to focus the imaging light and potentials directly onto the condensate formed. These components allow for the manipulation of the atom cloud during the experiment, which is a vital part of the measurements made. It is this feature that differentiates this cold atom experiment from other set-ups. The DMD will be discussed in depth later-on in section 2.4.

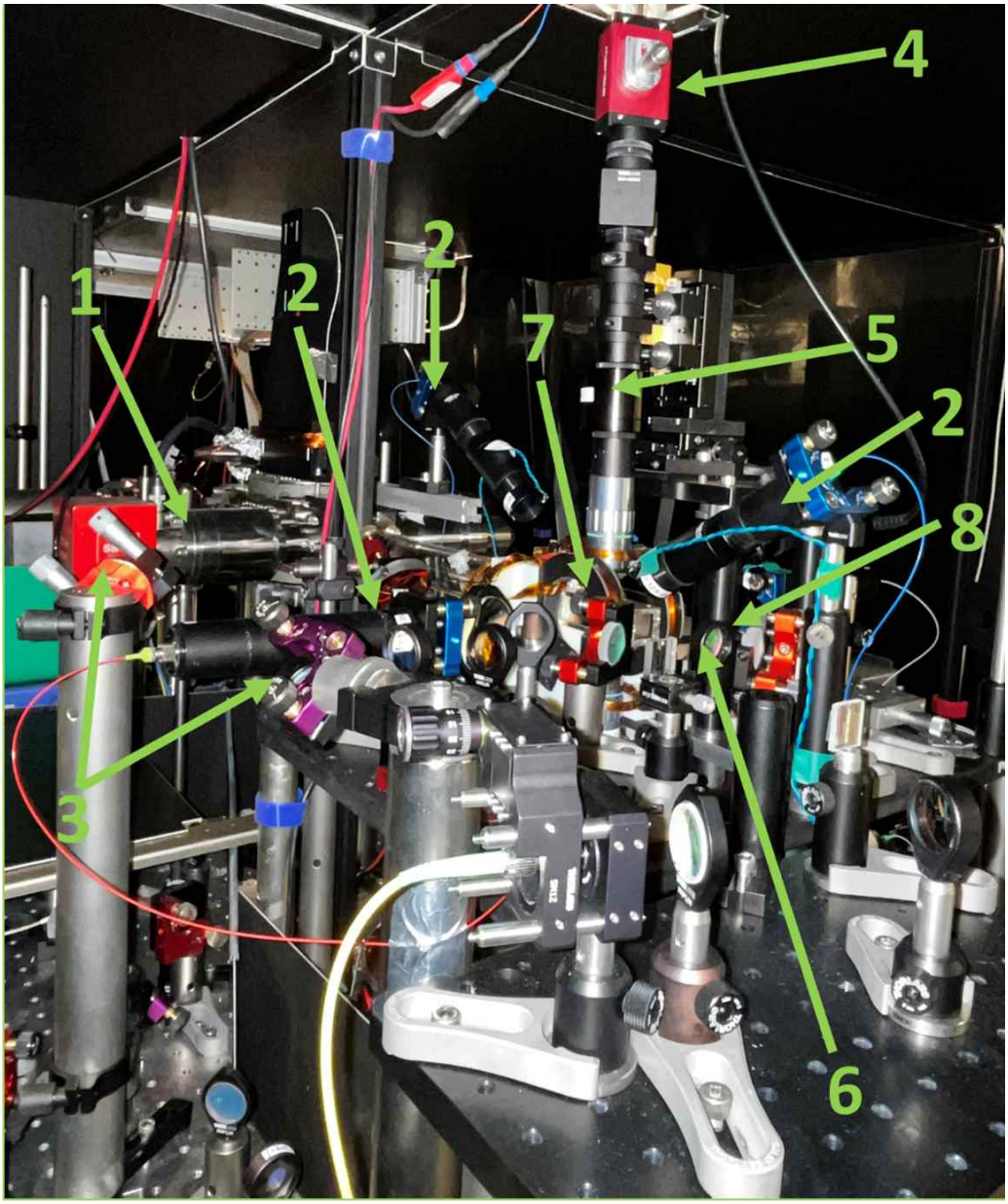

Figure 2.1: Image of the experimental step up with some of key components labelled, which will be discussed in detail later in the report 1) 2D MOT 2) 3D MOT Beams 3) Dipole Trap Beams 4) Vertical Camera 5) Imaging Objective 6) Flat Trap Beam 7) Science Cell 8) Imaging Beam.

2.2 Vacuum system

The experiment requires a vacuum system due to the extremely low temperatures and energies of the cold atoms produced. The atom cloud reaches temperatures as low as 10nK so any interaction with atoms in the air would disrupt the system with unwanted energy from collisions. The vacuum system is seperated into two chambers. There is the 2D MOT chamber which is made of titanium and is at a pressure of 10^{-7} mbar and a science chamber at a pressure of 10^{-10} mbar. The two chambers are connected by a 30 cm long glass tube.

Figure 2.2 displays an image of the vacuum system with the discussed components labelled. In the 2D MOT chamber the atoms are initially loaded into a trap. The pressure is higher in the 2D MOT chamber since a higher pressure increases the rate of atom loading and the purpose of the 2D MOT is to provide a good rate of atoms to the 3D MOT. This chamber has a window to allow for the optical access of the push beam which pushes the atoms through the vacuum system from the 2D MOT to the science chamber. At the centre of the science chamber the 3D MOT beams and the optical dipole trap beams intersect. This is where the BEC is formed. The two chambers are separated by a differential pumping stage which consists of a small tube that is 21 mm in length and has a diameter of 2.1 mm. This allows for the pressure difference of the two chambers to be maintained via an ion pump.

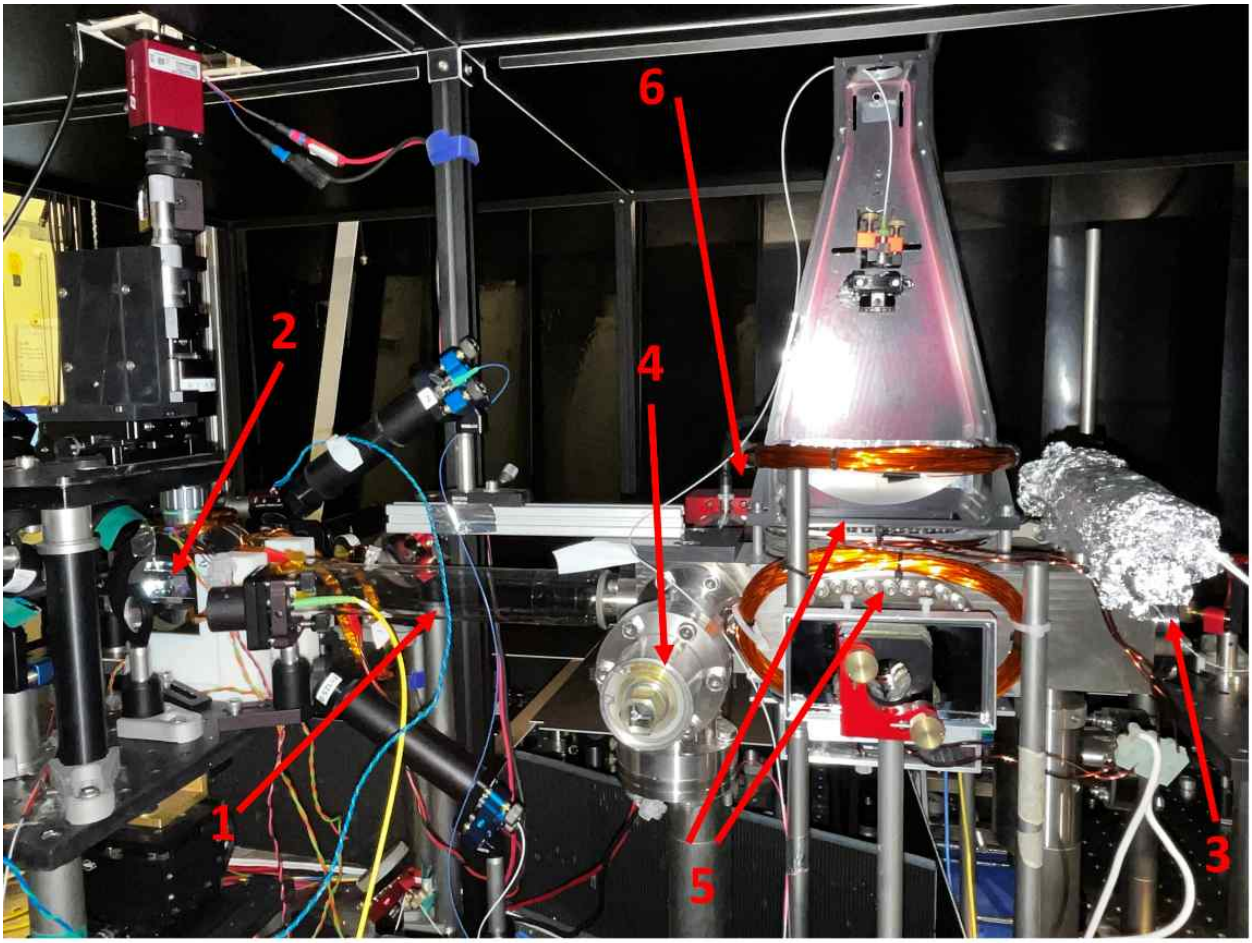

Figure 2.2: An image of the vacuum system along with surrounding components 1) Glass cell connecting the 2D MOT chamber to the science chamber 2) Science cell which is surrounded by the 3D MOT system. 3) The window at the back of the 2D MOT chamber which allows the push beam access 4) Connection between the glass cell and the 2D MOT where the differential pumping stage takes place. 5) Windows in the 2D MOT vacuum system 6) 2D MOT

2.3 Laser systems: Cooling, trapping, manipulating, and locking lasers

The laser systems in the experiment allow for the production of a Bose-Einstein Condensate through different cooling stages. The first stage of cooling happens in the 2D and 3D magnetic optical traps (MOT) and the second stage takes place in the optical dipole trap.

For each new project a new set of experimental parameters is required which includes different shapes, temperatures and atom numbers of the atomic cloud. For example, the investigation of the fountain effect required an elongated condensate cloud with a high atom number, whereas the work on 1-D dynamic potentials required a very cold, circular cloud with a low atom number. The alignment of the laser optics can be modified physically in combination with altering the powers and frequencies of the lasers with the control system. Modifying these parameters allow the temperature, atom number and shape of the cloud to be controlled. The condensate fraction can also be maximised.
The dipole trap has the biggest effect on these parameters and consists of two beams- a 1550 *nm* laser and a 1070 *nm* laser. The temperature and condensate fraction are mostly controlled by the final potential of the optical dipole trap which can be altered by changing the power at the end of the evaporation ramp using the control system. The temperature of the cloud can be decreased by ending the evaporation at lower powers since it means more atoms are evaporated. The shape of the dipole trap can be modified by altering the final ratio of the powers of the dipole trap beams in the control system. This means elongated BEC clouds can be created by having one of the beams in the dipole trap at a higher power. If the 1070 *nm* contributes more dominantly, the cloud of atoms is elongated in the horizontal direction since atoms are less trapped towards the centre of the trap and more towards the horizontal beams. A circular cloud is formed from having the 1070 *nm* and 1550 *nm* beams well focused and equally contributing to the trap depth by altering the powers accordingly.

In this section the stages of cooling will be discussed in detail, starting with the principle of a magneto optical trap, which is used in the 2D and 3D cooling stages along with the locking system used for the lasers to ensure that the wavelengths of the lasers in the 2D MOT stay correct.The optical dipole trap

system will then be discussed and how evaporative cooling takes place in this stage. The final part that will be discussed is how the atoms are manipulated using the DMD and imprinting laser.

2.3.1 Principle of a Magneto-optical trap

The first step to creating an ultra-cold cloud is to trap and cool the atoms. This takes place in a magneto optical trap, or a MOT. Using this technique, atoms at room temperature can be cooled down to temperatures as low as several microkelvin. A MOT consists of an intersection between six circularly polarised optical molasses beams, which are red detuned, and a weak, quadrupolar, spatially varying magnetic field, produced by anti-helmholtz coils. A basic diagram of this is shown in figure 2.3 with the relevant parts labelled.

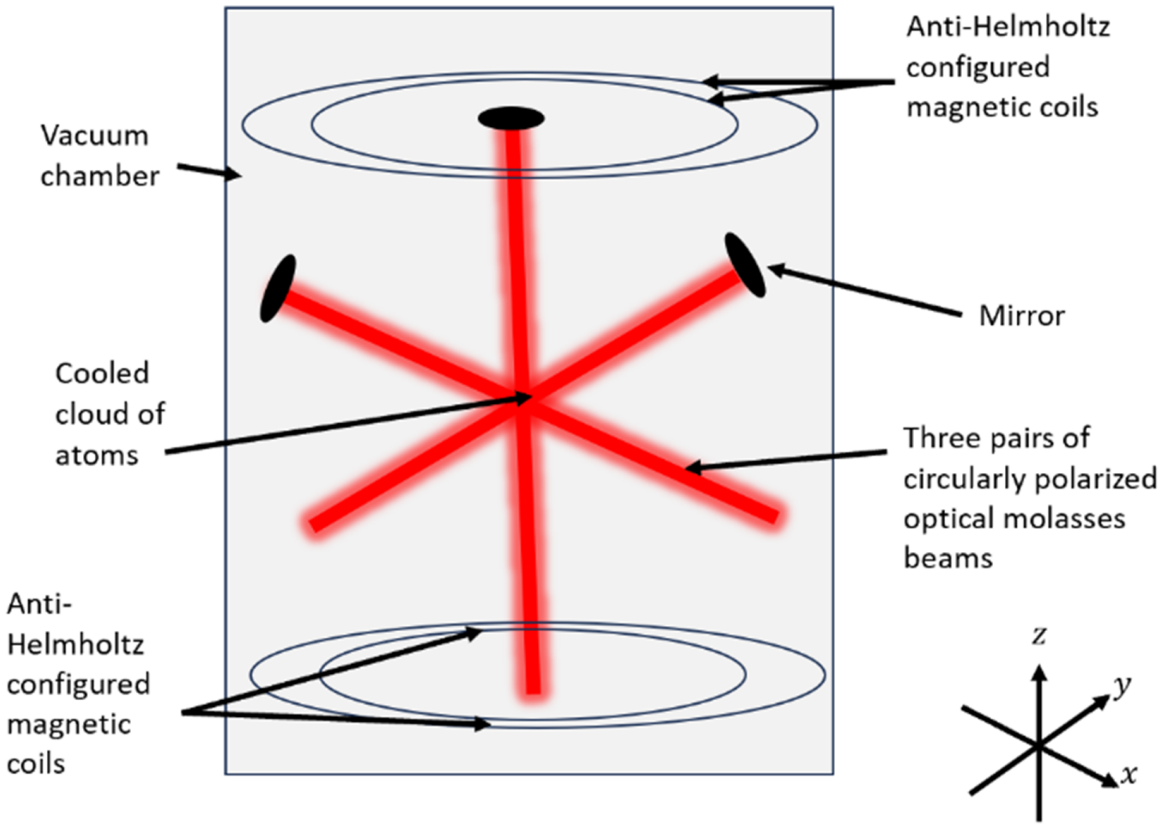

Figure 2.3: Basic diagram of the experimental set-up of a magneto-optical trap. The three pairs of optical molasses laser beams cross each other at the centre of the trap and the magnetic coils, in anti-Helmholtz configuration provides the quadrupole spatially varying magnetic field that is required for the trapping. The cooled atoms collect in the centre of the trap which is the midpoint between the pair of coils where the six beams intersect.

Laser cooling requires specific internal atomic transitions to allow for atoms to absorb photons from the optical molasses beams. The transition between the ground state and the excited state of an atom, can only take place when the light is detuned to a frequency a little less than the resonant frequency of the transition, known as red detuning. Since the atoms are moving, the light frequency is doppler-shifted either closer to or further from the transition frequency. The incoming photons from the incident laser will only be absorbed by atoms travelling towards the laser beam due to the detuning of the light.

When the atom absorbs the photon, there is increase in energy of the atom, by the photon energy, $\hbar\omega$, and momentum, $\hbar$k, as it is raised from ground state to this excited state. When the atom absorbs the photon, the atom gains the momentum from the photon. There is change in velocity of the atom, called the recoil velocity, V_R, during photon absorption in order for momentum to be conserved which is given by

$$V_R = \frac{\hbar k}{m}, \tag{2.1}$$

where m is the mass of the atom.

There is a probability that atoms in the excited state will decay back to ground state within a certain time period which can happen in two ways: stimulated emission and spontaneous emission. In stimulated emission the atom loses the momentum it has gained and there is no net change of momentum in the process. But if atoms undergo spontaneous emission, a photon which matches the energy of an incoming photon is emitted, but in a random direction. This in turn results in another momentum kick, $\hbar$k, for the atoms but also in a random direction. After many absorption/re-emission cycles, the random directions average out, resulting in the atoms gaining a net momentum change in the direction of beam propagation. This is because spontaneous emission is isotropic. Since the laser is red detuned from the energy transition of the atom, the atoms will experience a doppler shift towards the transition as they travel towards the beams and a doppler shift away from the transition when they are moving away from the beams. Since the average momentum kick is in the direction of the beam propagation, this results in a force on the atom as it moves towards the laser source- slowing them down and reducing the width of the velocity distribution of the atoms given by

$$V_{RM} = \sqrt{\frac{3k_BT}{m}}. \tag{2.2}$$

It is important to note that the spontaneous emission does not change the momentum of the atoms but leads to an indeterminable $< p^2 >$.

The force experienced by the atoms due to doppler cooling, F, is known as radiation pressure and is given by

$$\mathbf{F} = \hbar \mathbf{k} \Gamma \rho_{aa}, \tag{2.3}$$

where

Γ = Rate of decay

$\rho_{aa} = \frac{1}{2} \frac{I_R}{1+I_R+\frac{4}{\Gamma^2}(\triangle_{\text{eff}})}$

The atoms should be cooled in all directions so the frictional force should be experienced along all three Cartesian axes hence why the three pairs of orthogonal beams are used. Atoms will be slowed down (cooled) in all three spatial dimensions.

This configuration is known as an optical molasses and works by applying a radiation pressure, a force similar to drag and friction, to slow down the random movement of atoms and hence cools them. However, the force applied to the atoms for cooling is homogeneous and cannot trap the atoms.

In order to trap atoms at the crossing point of the optical molasses beams, a pair of magnetic coils are used in the anti-Helmholtz configuration, which provides a quadrupole magnetic field. The potential is given by

$$U = -\mu \mathbf{B(r)}, \tag{2.4}$$

where **B(r)** is the magnetic field strength of the quadrupole field.

In an anti-Helmholtz configuration current flow in the opposite direction in the coils and provides an inhomogeneous magnetic field. This results in a Zeeman shift in the m_f transition level which is proportional to the radial distance from the centre of trap and creates a force that acts towards the trap centre. The Zeeman effect is an analogous effect to the Stark effect, but instead of an electric field, the spectral lines split in the presence of a static magnetic field. Circularly polarised light $\sigma^{\pm}$ addresses transitions between Zeeman sublevels where for σ^{-} light, the atom will transition from m_F-> $m_F^{\pm}$. This is used in MOTs. As atoms move away from the centre of the trap, the $\sigma^{\pm}$ light will only address the

Zeeman level which has reducing energy for an increasing field strength. This results in an increased probability of photon absorption at distances further from the centre of the trap, meaning the force on atoms is stronger when they are moving faster, and are further from the centre of the trap.
It is important to note that there is a minimum possible temperature that atoms can reach in a MOT which is known as the recoil temperature, T_R. This temperature corresponds to the recoil energy that an atom gains when emitting a single photon and is given by

$$T_R = \frac{1}{k_B m}(\frac{hv}{c})^2. \tag{2.5}$$

Due to this, a MOT is usually used as a first step in a cooling process in experiments requiring ultra-cold temperatures to initially load and pre-cool the atoms.

In this experiment, both a 2D and 3D MOT are used to cool and trap atoms. These systems will be explained in the next section.

2.3.2 2D and 3D Cooling

There are two stages to the MOT in this experiment. The first stage is a 2D MOT, which has the primary function of providing the 3D MOT with an increased rate of cold atoms to be trapped (higher loading speed and larger number of atoms). Some of the differences between the 2D and 3D MOT are the respective vacuum systems the MOTs are positioned in as well as the fact the 3D MOT traps the atoms in all three spatial dimensions whereas the 2D MOT traps in only two directions.

The 2D MOT system consists of one MOT beam in the vertical axis and one MOT beam in the horizontal axis, which consist of combination of the cooling and repumper beams, with a power ratio of 2:1. The 2D MOT produces a cigar-shaped trap due to the cylindrical lenses that expand the beams. Since there is minimal confinement down the third axis, between the 2D chamber and the glass cell, the push beam is able to push the cooled atoms into the 3D MOT.

The atoms from the 2D MOT are moved through the glass cell to the 3D MOT. The 3D MOT is formed of three pairs of counter propagating beams as shown in figure 2.4, which means confinement

is achieved in all three axes, so the MOT is confined in all three spatial dimensions. In figure 2.4 there is a close-up image of the MOT visible in the science cell. It appears as a red oval shape and changes in this shape can give indications to any misalignment of beams in the 3D MOT. The vacuum system of the 3D MOT is formed inside of a glass cell meaning the atom cloud is easily accessible, and can be manipulated from a close distance. As well as this, beams, such as for the dipole trap, can be positioned much closer to the atoms. This is extremely beneficial for running experiments on the atom cloud.

The atoms are loaded for around 5 seconds from the 2D MOT to the 3D MOT. The loading time can be changed to increase/decrease the amount of atoms in the 3D MOT. Around 10 billion atoms are trapped in the 3D MOT and are cooled to around 350 μK. The temperature of the atoms in the 3D MOT can be decreased further by implementing a dark MOT stage. During the dark MOT, the cooling light is red detuned further to ensure that cooling is favoured over trapping. Simultaneously, the intensity of repumper light is reduced, to stop the atoms being pumped back into the excited state, so they fall back to their ground energy state. This reduces the potential of atom loss from collisional de-excitation. During the dark MOT stage, the temperature in the trap is reduced to round 50 μK. There is a minimum possible temperature that atoms can reach in a MOT, which is reached after the dark MOT stage atoms. At this point the atoms are at the coldest temperatures feasible in the 3D MOT. However, this temperature is still not cold enough for the atom cloud to form a BEC. For ultra-cold atomic temperatures to be reached the atoms must undergo evaporative cooling, which takes place in a crossed dipole trap.

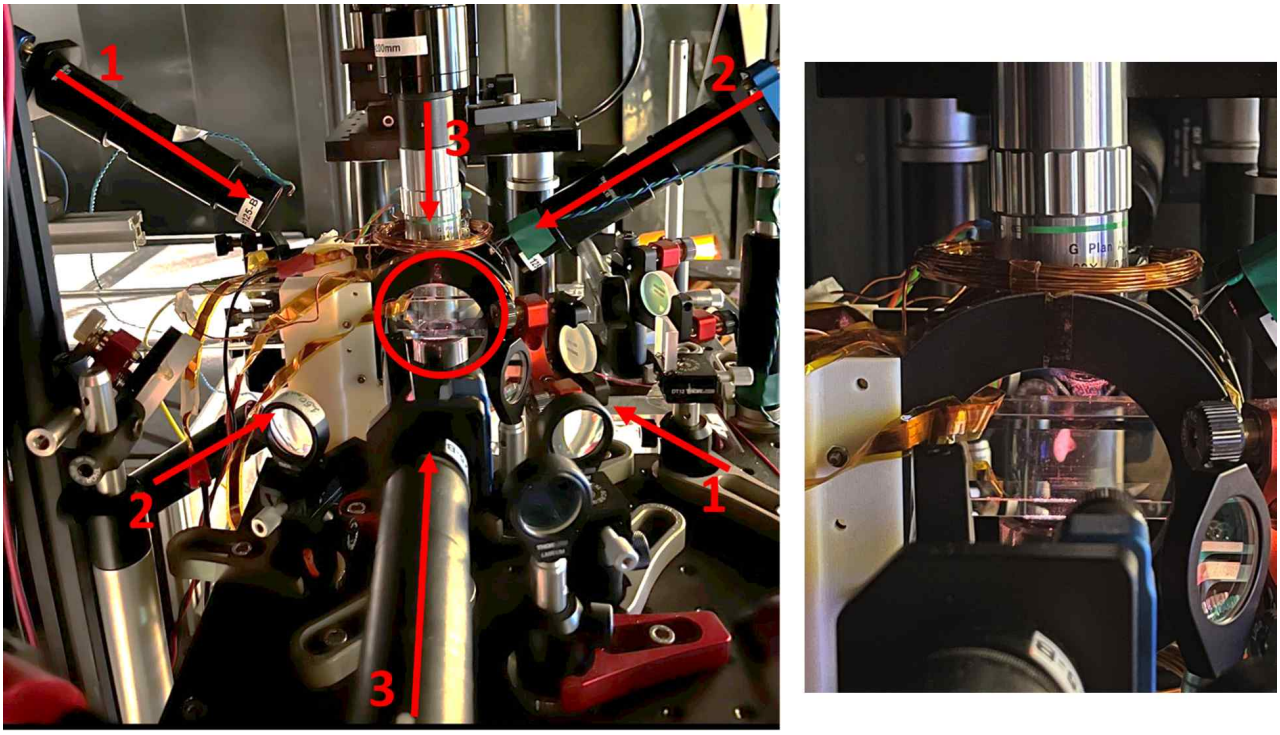

Figure 2.4: An image of the 3D MOT system shown on left where the pairs of vertical MOT beams are labelled as 1 and 2 and the pair of horizontal MOT beams are labelled as 3. The three pairs of beams point at the science cell circled in red and shown in a zoomed image on the right of the figure. The science cell sits between two anti-Helmholtz coils and the three pairs of beams point to the centre of it hence creating the magneto-optical trap.

2.3.3 Laser locking

The two MOTs consist of a cooling and repumper laser, both with a wavelength of 780 nm, which are provided by 2 Toptica DL Pro lasers. The two lasers along with the relevant optics are displayed in figure 2.5. The figure displays an optics diagram of the box which holds the repumper and cooling laser as well as the tapered amplifiers (TA), which are used in the amplifying systems and will also be discussed in this section. An active feedback loop system is required to lock the wavelength of the repumper and cooling lasers at specific transitions, so they do not drift during experimental sequences. The repumper laser is locked to the spectroscopy of ^{87}Rb at the repumper transition of the D2 line, F = 1 $\rightarrow$ F' = 2, while the cooling laser is locked to the cooling transition of ^{87}Rb. The cooling lock is derived from the repumper lock hence the laser system can be described in terms of slave and master lasers where the cooling and repumper are labelled respectively.

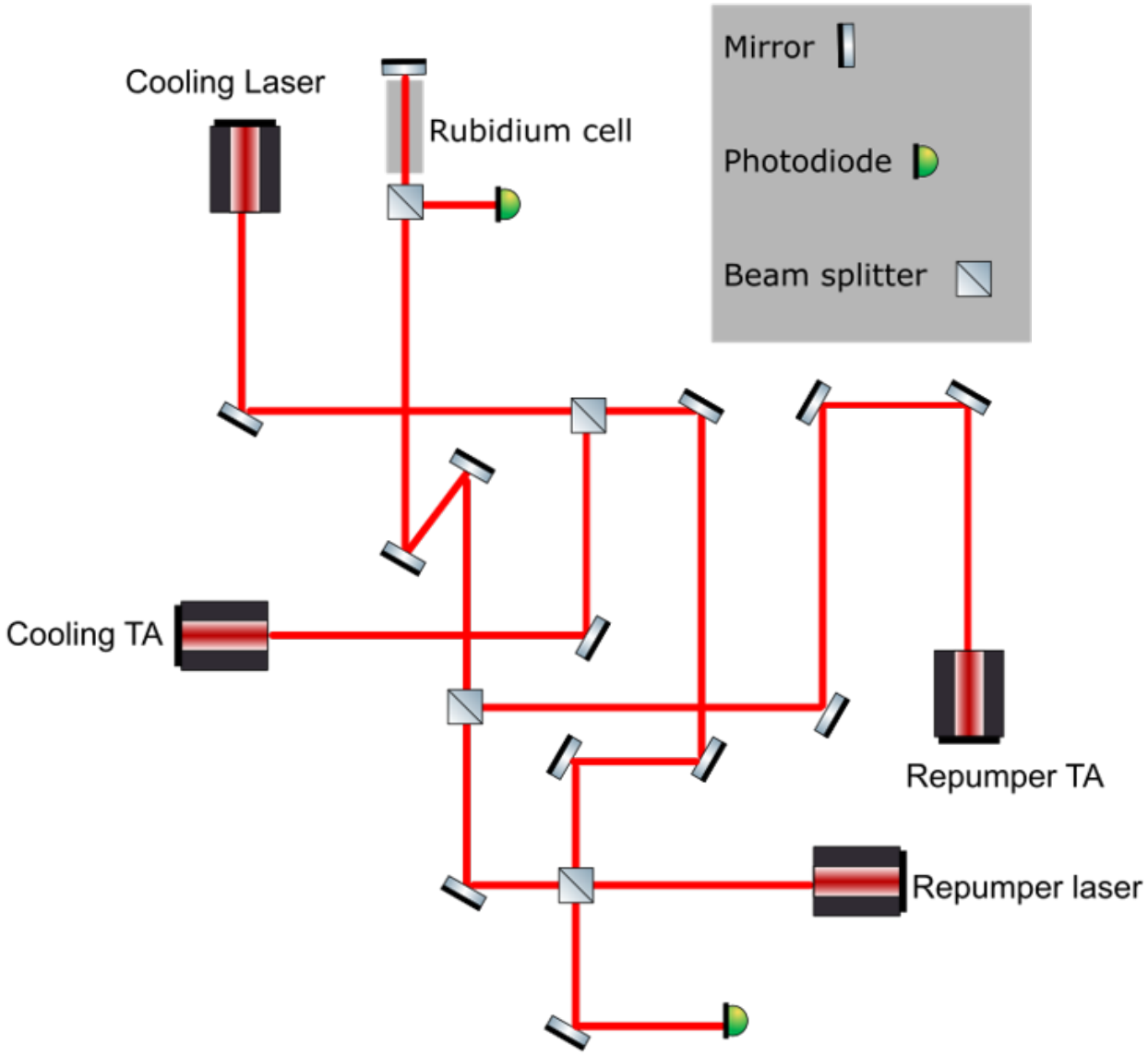

Figure 2.5: Diagram of the optical layout inside of the box that contains the repumper and cooling lasers, the locking system and the amplifyer system. This box contains two of the TAs used in the amplifying system. After amplification by a TA, the amplified laser light is passed through an AOM and then through a fibre, which transports the light into the relevant parts of the experiment.

One of the reasons alkali atoms are often used in cold atom experiments is because alkali atoms have closed transitions, which are necessary for laser cooling. It is for this reason that ^{87}Rb is used as the experimental species, in addition to the fact that ^{87}Rb has useful transitions at optical ranges around the 780 nm laser used for cooling and repumping the atoms. The transitions and relevant energy levels are summarized in figure 2.6 which shows the hyperfine structure for the $5^2S_{\frac{1}{2}}$, $5^2P_{\frac{1}{2}}$ and $5^2P_{\frac{3}{2}}$.

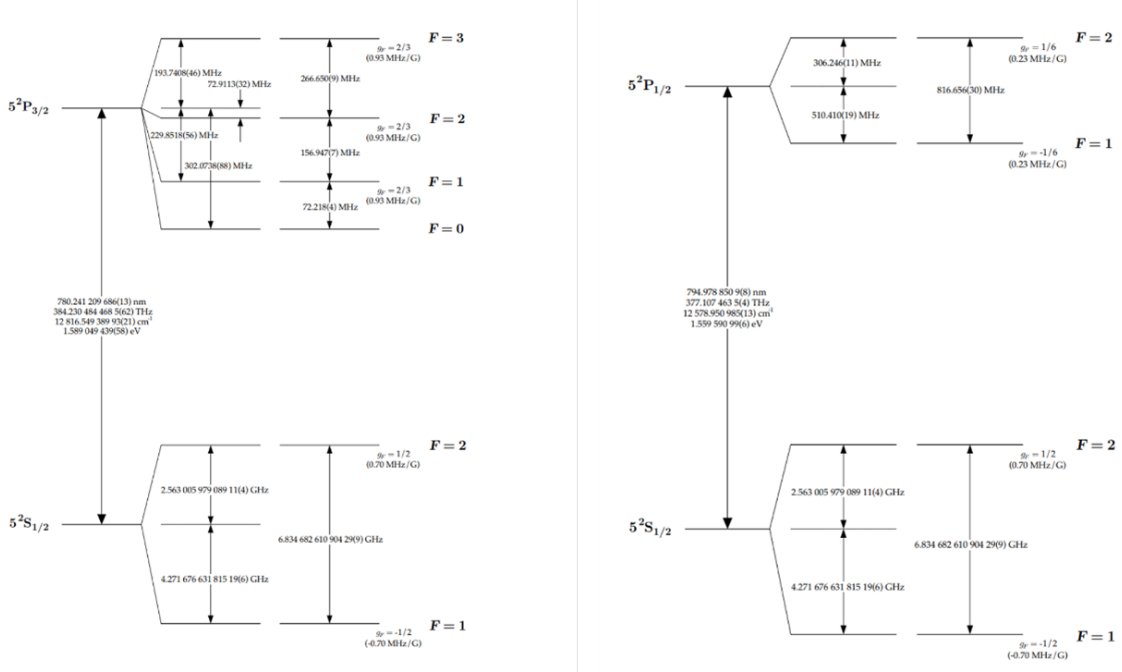

Figure 2.6: From [42] Displays the hyperfine structures for the $5^2S_{\frac{1}{2}}$, $5^2P_{\frac{1}{2}}$ and $5^2P_{\frac{3}{2}}$ levels of Rubidium-87 with relevant details such as frequency splitting, Lande g_f factors and Zeeman splitting's labelled. The diagram on the left shows the D_2 transition and the left is the D_1 transition.

The lasers are locked using the absorption spectrum of Rubidium-87 from the D2 line. The locking system has two lasers: repumper and cooling. The repumper laser is important as without it all the atoms would collect in the lower ground energy state since the repumper pumps atoms back into an excited state. Due to this, the repumper is kept at a constant frequency, which is on resonance with the F=1 $\rightarrow$ F'=2 transition of the D2 line. Figure 2.7 shows the position the repumper laser is locked at circled in red , which corresponds to the desired transition. It is important to also note that the a small amount of power from the repumper laser is directed into the spectroscopy set-up which is required for the absorption spectrum of the rubidium samples, as figure 2.5 shows. The cooling laser lock is found from the repumper laser which is locked at the repumper transition. It is found from a beat note which is created from the two lasers by overlapping 5 mW of each lasers onto a photodiode. A beat signal is produced from this where the two frequency components come from the sum and difference of the cooling and repumper laser frequencies. Since the cooling transition is 6.8 GHz away from the repumper transition, the cooling lock needs to be set so the frequency difference between the cooling and repumper lasers is 6.8 GHz. The beat signal is passed through a low pass filter and then

combined with a RF local oscillator frequency, which is fixed. The combined signal is passed through a synthesiser and another low pass filter. After this, the signals go into the error signal circuit board and are split into two branches. In one branch is a fixed attenuator which converts to a DC signal and in the other branch is a frequency dependent attenuator, created by a high pass filter. This also creates a DC signal. From this, the error signal found is fed back into the lock box. During a sequence, the frequency of the cooling light needs to change during the cooling processes, the dark MOT stage and for imaging. Due to this, the feedback loop, that keeps the locks fixed, adjusts throughout a sequence to ensure the cooling laser is kept locked to the required frequency. The error signal the cooling laser is locked to is displayed in figure 2.7 where the lock point is circled in red.

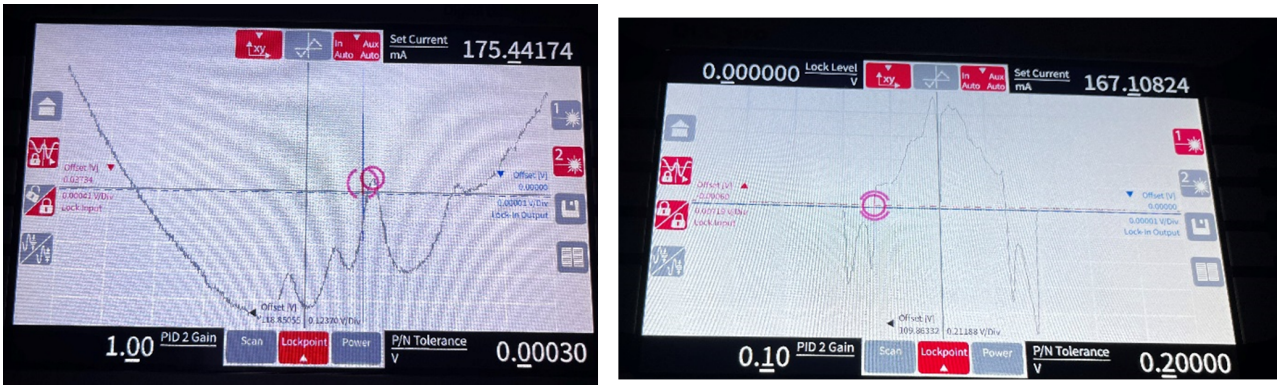

Figure 2.7: Images of the locking points for the repumper (a) and cooling (b) laser for the D2 transition. The repumper laser is locked to position of the fourth peak, circled in red. This peak corresponds to the repumper transition F=1 $\rightarrow$ F'=2. The cooling laser is locked to an error signal where the lock point is once again circled in red. When the signal is locked at this position, the frequency of the locked laser is at the cooling transition.

Once the lasers have been locked, it is important that they supply appropriate power to the MOTs. This is done by amplifying the power of the lasers since, without amplification, the powers would not be sufficient enough to produce the size of MOT required in the experiment. Powers of lasers can be amplified using a TA and figure 2.5 highlights the optical paths for two of the TAs used in this experiment since the second cooling TA resides in another optics box.

The first cooling TA is a modified Newport TA (TA-7613) and provides an amplified power of 600 mW, which provides laser light for the imaging, 3D cooling, push beam (350 uW) and the input to the second cooling TA. This TA is also a Newport TA and provides power to both the horizontal and

vertical cooling in the 2D MOT. Finally the repumper TA, shown in figure 2.5, amplifies the power of the repumper laser for both the 2D and 3D MOT.

Laser locking is a key step in the experiment as it helps to provide the MOT systems with the lasers required to cool the atoms.

2.3.4 Crossed Beam dipole Trap

To reach the ultra-cold temperatures as well as the high phase space density required to form a BEC, a crossed dipole trap is used. It consists of two red detuned lasers at wavelengths of 1550 nm and 1070 nm, which cross at the centre of the 3D MOT. The two lasers are detuned far from the atomic transition of ^{87}Rb to minimise heating effects and have different wavelengths to avoid any interference between them. Both high power lasers are passed through AOMs (acousto-optic modulator) which are used to adjust the power of the laser beams during an experimental sequence. This is beneficial as the trapping frequency and potential of the trap can be easily altered during a sequence to change the shape, temperature or number of atoms in the cloud depending on what experimental parameters are required.

The dipole trap works through a similar principle as optical dynamic potentials via the AC stark effect. Since the beams are red detuned and have a gaussian profile, the atom cloud experiences a force towards the highest intensity region of the beam, which is at the centre. The two red detuned lasers overlap at the centre creating a tight confinement in every axial direction.

The powers of the dipole trap beams are exponentially ramped down which forces the atoms to undergo evaporation from a few hundred microkelvin to a few hundred nanokelvin. This process is known as evaporating cooling. When this takes place, the highest energy atoms leave the trap and if the process is done slow enough, the atoms will re-thermalise to a lower temperature before the next highest energy atoms leave the trap. This cycle repeats until around 99 % of atoms from the trap are lost, leaving ultra-cold atoms at temperatures as low as 10 nK. Since the atoms are situated in the centre of the beams, the Gaussian profiles are approximated as quadratics, so the trapping potential can be

treated as harmonic, as described by

$$v(r) = \frac{1}{2} m\omega^2 r^2. \tag{2.6}$$

Figure 2.8 is a basic image of the Gaussian profiles where the blue is the condensed component of the cloud, and the red is the thermal component. The ratio of the powers between the 1550 nm and 1070 nm lasers can be changed which alters the trapping frequency of the harmonic. The trapping frequencies alter the confinement of the trap, so a higher trapping frequency means a tighter confinement and lower means a shallower confinement.

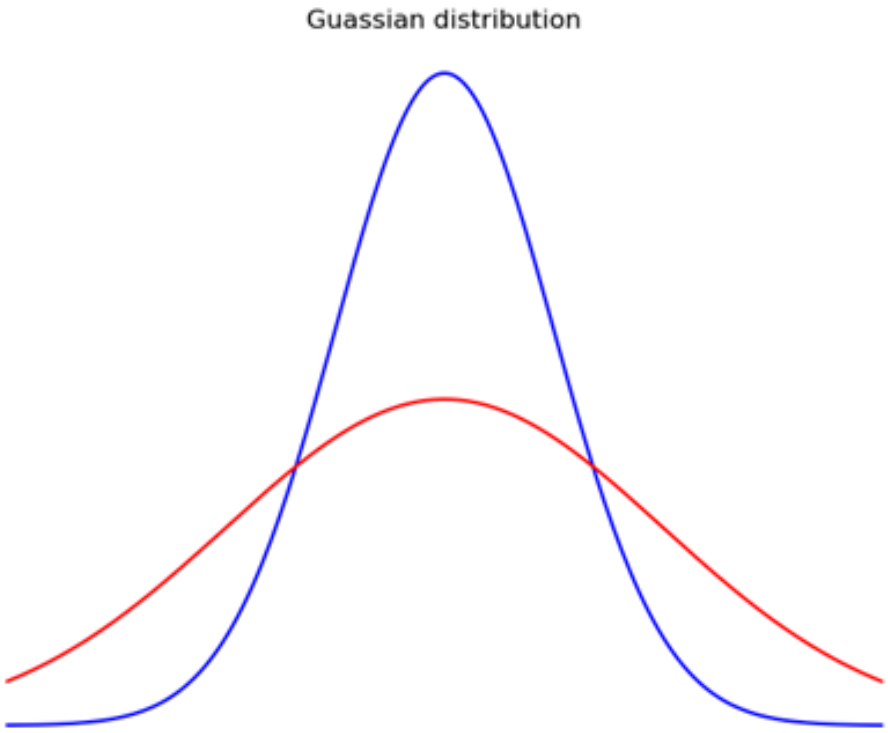

Figure 2.8: An image of the Gaussian distribution of the cloud of atoms, where the blue is the condensed component of the cloud, and the red is the thermal component.

2.4 Optical Potentials

The most important aspect of the experiment the is generation of optical potentials via a DMD which allows for the manipulation of the ultra-cold atoms, which have been generated via the above methods. The DMD is illuminated by an imprinting laser diode and a desired image is shaped and reflected into

the optical system and onto the atoms. Both the DMD and imprinting laser will be discussed below. Figure 2.9 is an optical diagram for the basic set-up of the imprinting laser diode and DMD. It follows the path of the laser light from the laser diode to the DMD and then finally to the microscope objective where the laser light is focused onto the atoms.

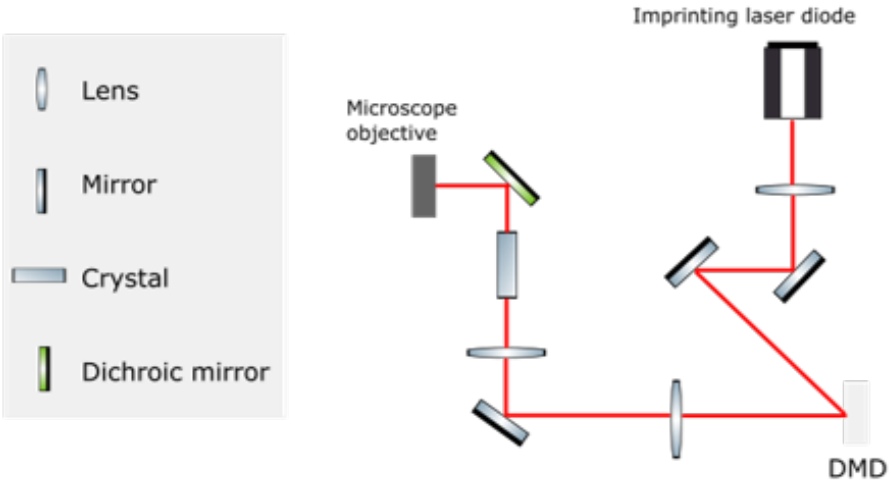

Figure 2.9: Optical diagram for the basic set-up of the imprinting laser diode and DMD

2.4.1 Digital Micro-mirror device (DMD)

A DMD is a type of spatial light modulator (SLM) device that contains an array of highly reflective micromirrors, which allow for customised images to be projected as the micro-mirrors can be rotated to change pixel brightness to display a desired pattern. The DMD is an integral part of the experiment as it allows for the manipulation of ^{87}Rb atoms using dynamic and static optical potentials.

In the experiment a DLP9500 digital micro-mirror device is used with an array of 1920 x 1080 micro-mirrors, each being 10.8 μm x 10.8 μm. This results in a total size of 1.1 cm × 2.1 cm. The DMD has a refresh rate of 10 kHz which means images can be changed every 100 μs. Figure 2.10 shows the DMD in position in the experiment (a) as well as a close-up image of the DMD used (b). The micromirrors can be individually rotated and flip between 'on' and 'off'. At the 'on' position light passes along the aligned beam path of the optical system, which makes the pixel appear bright on the

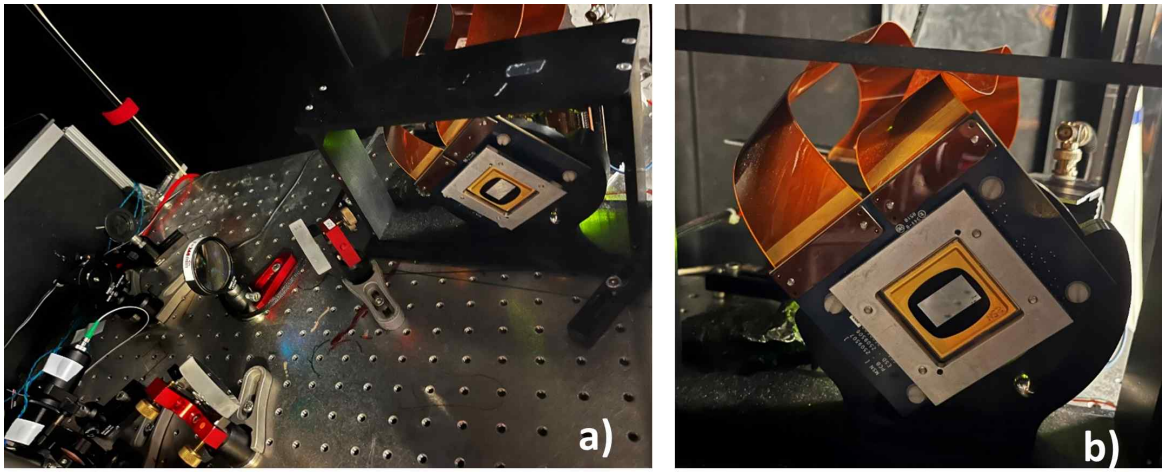

Figure 2.10: Position of the DMD in the experiment (a) as well as a close-up image of the DMD used (b).

screen. In the 'off' position the mirrors are flipped and the light that hits them no longer follows the desired beam path and the light is directed elsewhere, which results in the pixel appearing dark.

The DMD is supplied black and white bitmap images (e.g. X.bmp) with each pixel from the data equating to one micromirror. A white pixel means mirrors are flipped in the 'on' position and a black pixel means the mirrors are flipped in the 'off' position. Figure 2.11 shows a close-up image of the DMD flipped into the 'on' position at ±10 degrees (a) and in the 'off' position at ∓10 degrees (b). (The actual DMD used has an angle of 12 degrees). The DMD can provide both static and dynamic potentials depending on if a single image is supplied (static) or a sequence of images from a folder (dynamic) is supplied. When a folder is supplied, the sequence of images proceeds from one to the other by supplying a TTL signal, [43] (transistor-transistor-logic signal). This can be done in two ways: either directly from the control system or using a function generator which supplies signals at a fixed frequency. This is how patterns are built up from the light to create dynamics that manipulate the BEC in the experiment. This can be extended to grey scale images. To produce grey-scale the mirrors are turned 'on' and 'off' very quickly and the ratio of the 'on' to 'off' time determines the shade of the grey-scale produced. This method is called 'dithering'.

When the DMD is in use, the light from the imprinting beam, which will be discussed in the next section, illuminates it entirely and the desired image is shaped and reflected into the optical system. Figure 2.9 is a basic optical diagram showing the path of the laser light during this stage of the

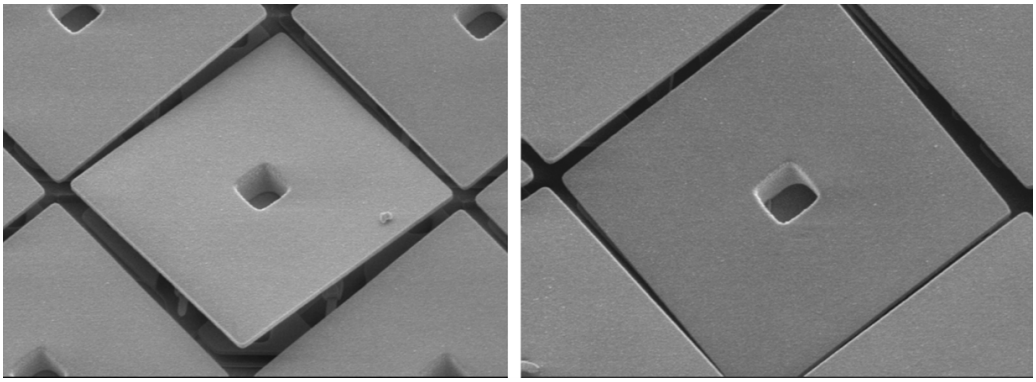

Figure 2.11: A close-up image of the DMD taken from [44] flipped into the 'on' position at ±10 degrees (a) and in the 'off' position at ∓10 degrees (b). (The actual DMD used has an angle of 12 degrees).

experiment. The light travels from the imprinting laser to the DMD then from here it passes through a telescope, crystal prism and dichroic mirror before combining with the imaging beam at the microscope objective where it is focused onto the atoms which allows for direct manipulation of the atom cloud to simulate quantum effects.

It is important to ensure that the distance between the microscope objective and the cloud of atoms is set correctly or the images on the atoms may be blurry and unfocused resulting in atoms not responding to potentials effectively. This is done by first focusing the top objective on the atoms. Then an image from the DMD is projected onto a CCD (charge-coupled device) through the lower image objective. The position of the lower objective can be adjusted until the image is well focused onto the DMD. Figure 2.12 is an example of an image that can be used to help focus the DMD. As the image shows when the objectives are positioned correctly the image produced by the DMD onto the atoms is clear. By focusing the DMD using the objectives it ensures that everything is in the same plane, i.e. the DMD projection is the same plane as the imaging system which is in the same plane as the cloud of atoms.

2.4.2 Imprinting laser

The previous imprinting laser used in the experiment was a tuneable infra-red laser. However due to the heating effect, caused by small detunings from this later, has recently been changed to a red laser with a much higher power and a larger detuning from resonance. The high heating effect of

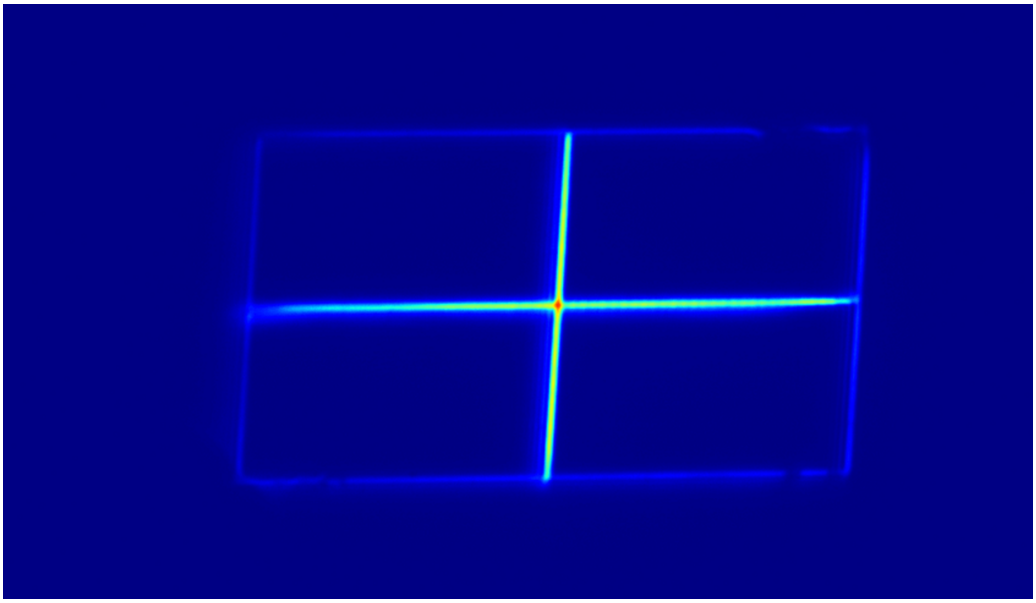

Figure 2.12: An example of an image that is used to focus the DMD.

the tuneable laser had meant measurements and experiments involving longer projection times were often not feasible as experimental parameters needed for such experiments could not be achieved. To overcome these issues a new red laser diode, model number M1F4S22-675.5-10C-SS5.2M2P19T3, purchased from Coherent, was installed. The new laser diode has central wavelength of 674nm and can produce up to 16 W. Unlike the previous laser, this laser is not tuneable, which should not be an issue since it is far enough detuned (blue detuning) from transition that heating effects should be negligible. Due to the large detuning, to achieve the same potential as the previous laser, the intensity required is 22 times higher. This means that the laser diode produces a large heat output. To manage this the laser diode is fixed onto a peltier module which itself is mounted onto a large heat sink. This combination maintains the temperature of the laser diode when it is in use. The peltier is controlled by a PID (proportional–integral–derivative) temperature controller.

The new laser diode is able to supply more power than the previous laser, so the optics were adjusted from the previous set-up so the beam of the laser diode expands in way that only the small central part of the laser is incident on the DMD. This is beneficial as it means the images generated by the DMD are better quality since the beam is more uniform.

2.5 Imaging

The atoms in the experiment are imaged by absorption imaging, which is a destructive process that works since a shadow of the light is left behind after the cloud is destroyed. As a quick summary in absorption imaging, light resonant to the cooling transition is absorbed by the cloud of atoms which increases their energy and destroys the BEC. However, the atom cloud leaves a shadow in the light beam which the CCD in the imaging system can pick up. This shadow signature is analysed and a colourised image of condensate cloud is produced, shown in figure 2.13. More details on how absorption imaging is used to image ultra-cold atoms can be found in [45].

Included in the experimental set-up are two absorption imaging systems, one horizontal and the other vertical. The first camera is an Allied Vision Mako G-125B (5054)-DEV000F315B95B0 and images the atoms from the horizontal direction, typically at a time of flight (TOF) of 25 ms. Figure 2.13 shows an image of the atoms pictured in TOF labelled a). The horizontal camera is used to measure the atom number and temperature of the cloud. The second camera takes images of the atoms from the vertical direction and is an Allied Vision Manta G-235B (E0020572)-DEV00F314D25CF . The vertical camera is extremely important as it is using this camera the images imprinted by the DMD onto the atom cloud can be seen. Figure 2.13 label b) shows an image of an elongated cloud atoms pictured in the vertical camera. The vertical camera is made from a series of two microscope objectives. One of the objectives focuses light onto the atomic sample and the other objective forms the image. It has a higher magnification than the horizontal camera.

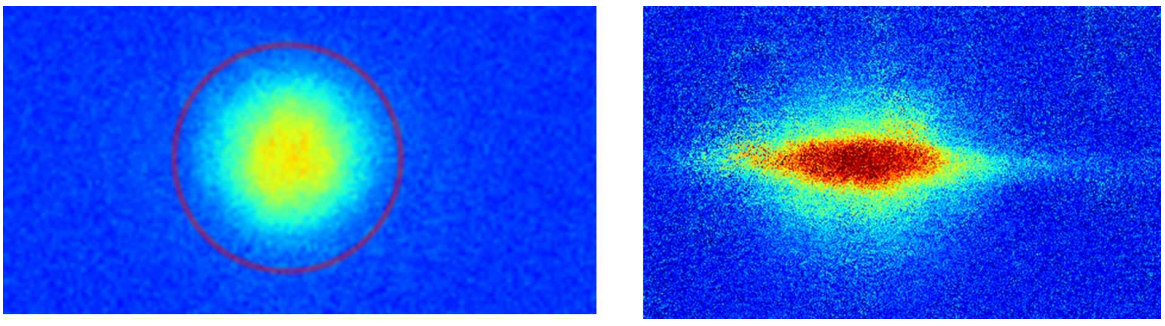

Figure 2.13: Absorption images of the atom cloud taken in a) 25ms Time of Flight expansion by the horizontal camera and b) In trap by the vertical camera with no expansion.

2.6 Control system and experimental sequence

In the control system of the experiment, different experimental parameters are controlled, such as laser powers and the times in which the lasers are switched on/off. This is to carry out experimental sequences on the system. Cicero Word Generator/Atticus are used as the control software for the experiment along with a National Instruments (NI) PXIe-1062Q chassis housing three cards- PXIe-8360, PXI-6713 and PXIe-6535, [46]. These interact with the control system through digital and analogue signals which controls shutters (opening/closing to allow laser light through), controls AOMs (control power of laser in a desired location) and triggers components, such as the DMD and cameras. The experimental sequences are created on Cicero. To avoid overfilling the buffers of the NI cards, the rate of the samples produced can be adjusted. From speeds of up to 1 MHz when necessary and, for longer stages with less changes, speeds of 1 Hz. This is done through a Opal Kelly XEM3001 FPGA which creates a flexible timebase.

The MOT loading stage is the first step of a sequence, which lasts for 5 seconds and is where the atoms are loaded from the 2D MOT to the 3D MOT (all while being laser cooled). The next stage is the dark MOT where the power of the repumper laser is reduced so the atoms drop back down to the ground state. This is when the 1070 nm and 1550 nm lasers are turned on, forming the optical dipole trap. The final stage of cooling, evaporative cooling, takes place next and the power of the dipole lasers is ramped down so a BEC is formed and held inside of the optical trap. The atoms are imaged by using the cameras to take three separate images which are averaged into a single image. Additional stages can be added to manipulate the atoms or to obtain information about the atoms. For example, triggering the imprinting laser and DMD at the end of the evaporation step, the atom cloud can be forced to interact with dynamic potentials from the DMD.

Each step of the sequence is broken up into different time frames which can be lengthened or shortened to change the size/shape of the atom cloud. If the evaporation steps are shortened, the cloud will be more thermal. This can be used to check the alignment of the experiment. The evaporation time can be reduced until atoms are seen, and then the alignment of the dipole cross can be improved so atoms are seen at longer times.

Chapter 3

Fermi Acceleration

3.1 Theory

Fermi acceleration [47] is a mechanism proposed by Enrico Fermi in 1949 as a way to explain high energy cosmic rays (heating of cosmic rays). It has great importance in astrophysical shock-wave events [48, 49], like supernovae, [50] since it explains the mechanism by which particles gain non-thermal energies. Fermi proposed this mechanism after observing the energies of charged particles after repeated reflection by a magnetic field, often referred to as a magnetic 'mirror'. The loss or gain in the particle energy depended on whether the magnetic 'mirror' was approaching the particles or moving away from them respectively. Using this as his basis, Fermi argued that since the probability of a head-on collision is greater than the probability of a head-tail collision therefore particles experience acceleration on average. This explains the abundance of high energy particles in space.

There are two types of Fermi acceleration: first-order and second-order, [51] [52]. First-order Fermi acceleration occurs in shocks (astrophysical shocks are caused by a supernovae) whereas second-order Fermi acceleration occurs in the environment of the magnetised cloud (moving magnetic mirror). The experiment simulates first-order Fermi acceleration, associated with cosmic rays, [53].

3.2 Experimental Set-Up

In the experiment a one-dimensional dynamic potential is created, using a DMD, which drives cold atoms in an optical lattice toward a barrier. In brief, the atoms are essentially dragged by the optical lattice up the harmonic trap until they reach the barrier where they undergo Fermi acceleration and are reflected.

To explore the effect, the experiment was set up, sketched in figure 3.1. Ultra cold atoms are first produced in an elongated 3D harmonic trap to create a thermal cloud. Along the weak trap axis, x, the atoms are loaded in a moving 1-D sinusoidal potential, which is shown by the arrow in figure 3.1. In the two other axial directions the potential remains harmonic. The atoms are kept in a tight binding regime at J=0 because the height of the potentials are at much higher temperatures than the thermal cloud of atoms. The DMD is used to generate two barriers at either side of the potential. The barriers are kept the same distance apart at 100×10^{-6} m.

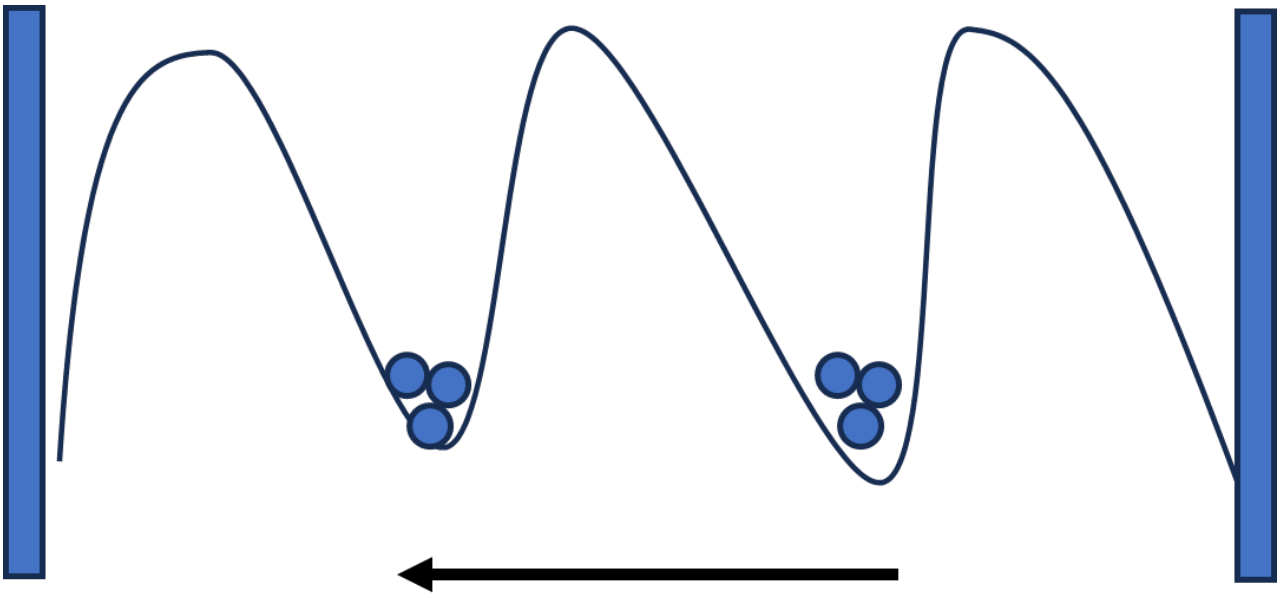

Figure 3.1: Sketch of the experiment with the two barriers represented by the blue rectangles. First, an ultracold sample of atoms, which sit in the potential wells, is produced. The periodic potential created by the DMD is loaded and put into motion, represented by the arrow pointing left.

The potential is generated using the DMD and projected onto the cloud of atoms in the x direction using the beam of the imprinting laser. Figure 3.2 is an example pattern used in a sequence where brighter regions correspond to higher potentials due to the grey scaling. Patterns, such as these in

figure 3.2, are fed into the DMD, and subsequently onto the atoms, at a rate of 0.4 kHz to 6kHz. This creates a moving periodic potential, which can be described by

$$F(x) = \frac{1}{2}A(1 + \cos(-\Omega t + 2\pi\phi x)) \tag{3.1}$$

Where:

A = Potential Amplitude

$\Omega = 2\pi$/t (driving frequency)

t = Time

ϕ = Wavenumber

x = Position

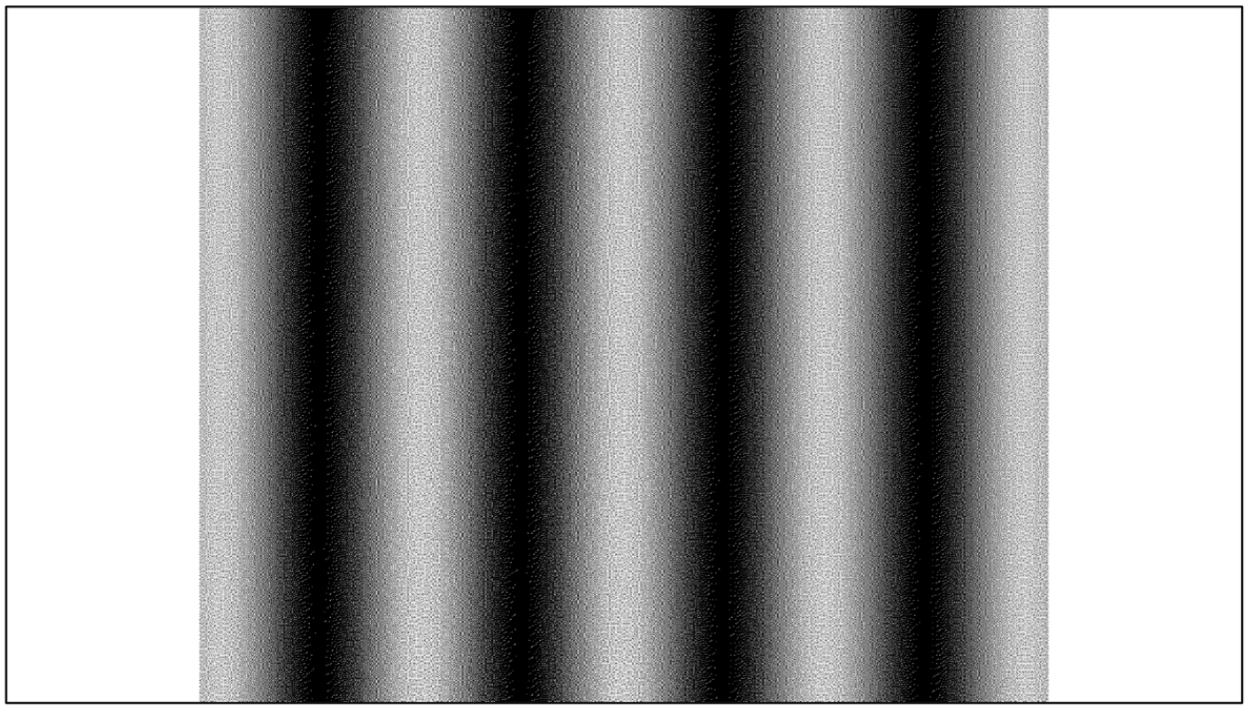

Figure 3.2: Snapshot of the DMD image produced that is then shone on the atoms to create the dynamic potential. The white parts at the end are the barriers.

Before changing any experimental parameters, the dynamic potential was first applied to the thermal atoms with no barriers. This was to compare how this differed from the observed effect with the barriers. In this case the atoms simply go to one side and leave the trap as expected.

3.3 Experimental Parameters

Initially, the experiment began with changing three main parameters and observing how the acceleration of the particles varied with these changes, if at all. The main focus was looking to see at which values of the parameters the acceleration is observed and at which values the atoms either dispersed or did not reflect. These initial observations were carried out with some fixed experimental parameters which are displayed in Table 3.1.

Table 3.1: Table of the fixed experimental parameters.

Distance Between the Barriers	$100 \times 10^{-6}\ m$
Potential depth of the Imprinting Beam	$8.09 \times 10^{-7}\ K$
Number of Atoms	$25k$
Temperature of the Cloud	$15nK$
f_x	17.5 Hz
f_y	151.5 Hz
f_z	73.2 Hz

Driving frequency, Ω

The driving frequency, Ω is the frequency at which the pattern is driven horizontally across the cloud of atoms. In this experiment Ω' is the refresh rate of the DMD, which can be directly changed using a function generator. There is a fixed relationship between Ω and Ω' given by,

$$\Omega = \frac{\pi\Omega'}{10} \tag{3.2}$$

Due to this, by changing the refresh rate of the DMD, Ω', the value of Ω can be varied for the experiment.

The effect is seen very nicely at certain frequency values as shown in figure 3.3. The acceleration of the particles from the barrier is best observed from 1 kHz to 4 kHz and the atoms can be clearly seen colliding with the left side of the barrier and then reflecting towards the right side of the barriers. On some of the images, there are two or more paths of atoms seen and the reasons for this is that the nature of the potential causes the thermal cloud to split among minima. The number of splits increases as frequency increases. At lower frequencies, the effect is not apparent as the atoms seem to just slam to

one side of the barriers and wait there or start to disperse which can be seen at 0.4 kHz in figure 3.3. At higher frequencies the cloud gets destroyed very quickly as seen at 6 kHz. Increasing frequency much higher than this also shows the atoms being dissipated before they have a chance to reach the barrier.

Wavenumber, ϕ

Wavenumber describes the spatial frequency of a wave over a defined unit of distance and is proportional to the frequency of the wave. A high wavenumber means higher frequency and a higher number of waves. The relationship between wavenumber, ϕ, and wavelength, λ, is given by

$$\phi = \frac{2\pi}{\lambda}. \tag{3.3}$$

When the value of ϕ is changed, it directly changes the pattern being projected by the DMD. The effect is observed the clearest at $42 \times 10^3\ m^{-1}$. At higher ϕ values, there is no apparent effect and the cloud of atoms appears not to move, as shown in figure 3.4. While the cloud is destroyed at higher frequencies, there is no observable effect at higher wavenumbers. It was expected that over longer time periods, the cloud would move at higher wavenumbers, but it was instead observed that with a higher wavenumber, the atoms remained undisturbed regardless of the timescales used in the investigation.

Dynamic potential amplitude, A

A is the amplitude of the dynamic potential hence is the height of the optical lattice amplitude. As expected, at lower A values, the reflection of the atoms is not observed since at lower values of A the potential does not have the energy to push the atom cloud up the harmonic. Initially, for higher values of A, the reflection of atoms is noticeably larger, until much larger amplitude values, whereupon the atoms are expelled quickly therefore destroying the cloud, as shown in figure 3.5.

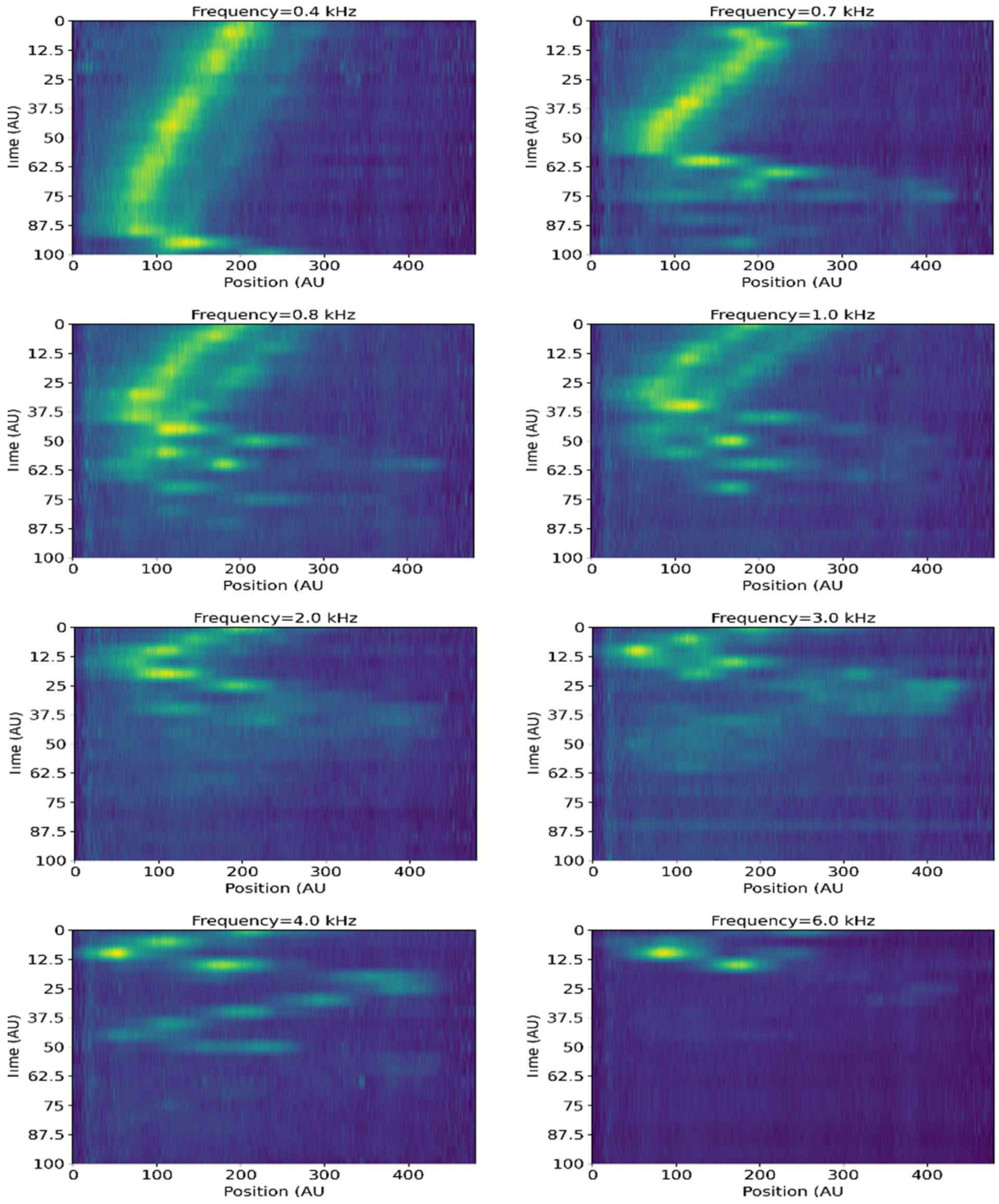

Figure 3.3: Integrated density profiles of a BEC under action of a one-dimensional periodic potential, at different values of Ω'. The x axis displays the position of the atom cloud in pixels and the y axis is the time in ms. An image is taken every 5 ms from 0-100 ms.

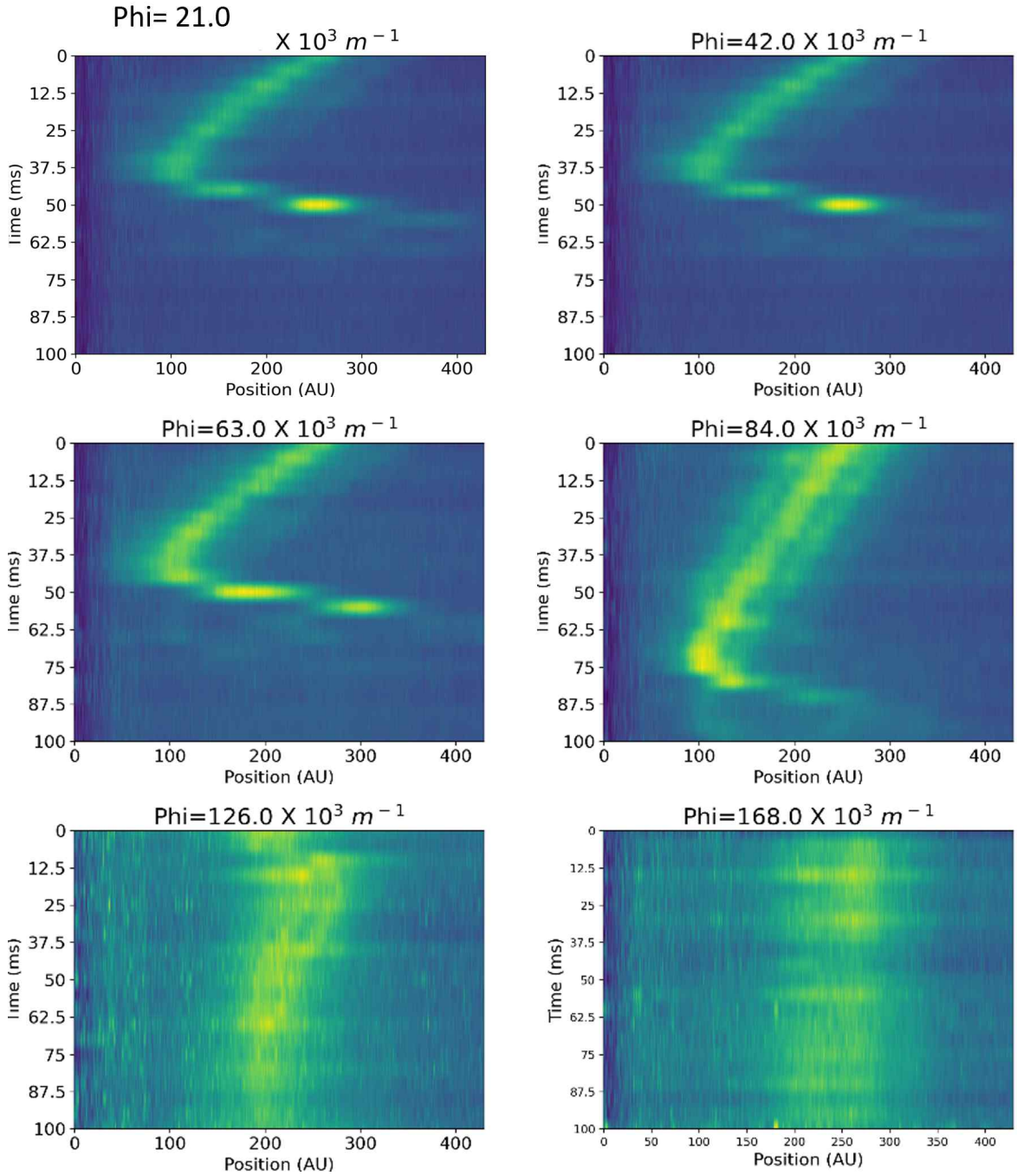

Figure 3.4: Integrated density profiles of a BEC under action of a one-dimensional periodic potential, at different values of ϕ. The x axis displays the position of the atom cloud in pixels and the y axis is the time in ms. An image is taken every 5 ms from 0-100 ms.

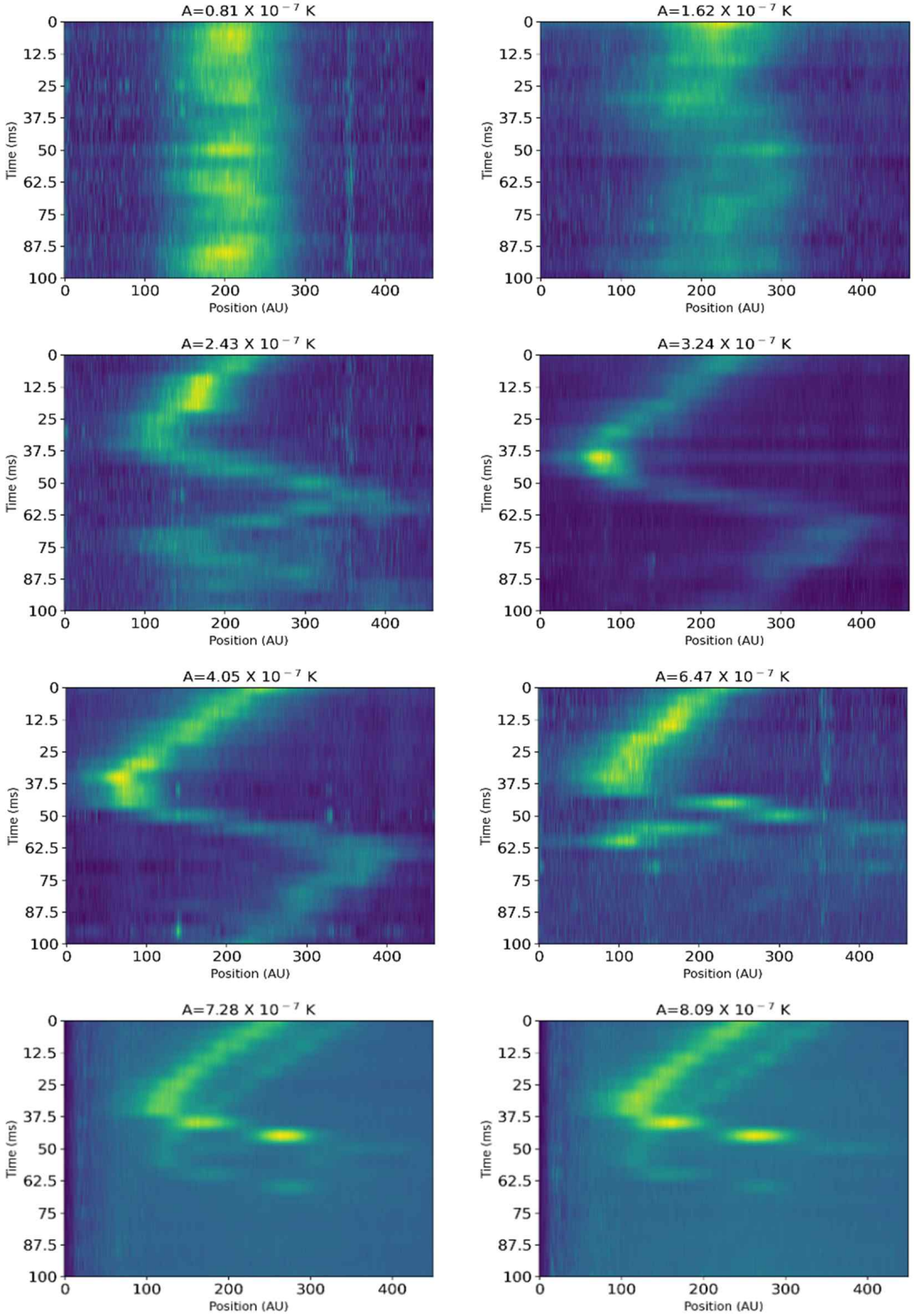

Figure 3.5: Integrated density profiles of a BEC under action of a one-dimensional periodic potential, at different values of A. The x axis displays the position of the atom cloud in pixels and the y axis is the time in ms. An image is taken every 5 ms from 0-100 ms.

From the above investigation, the optimal experimental parameters are displayed in table 3.2. At these parameter values, the atoms accelerate and reflect clearly. These parameters have therefore been fixed for future investigations of the effect.

Table 3.2: Table of the optimal experimental parameters.

Ω	100π Hz
Ω'	1×10^3 Hz
ϕ	$42 \times 10^3\ m^{-1}$
A	6.47×10^{-7} K

3.4 Velocity of the Atoms

In the experiment, the atoms are initially dragged by the moving sinusoidal potential at a velocity given by

$$v_i = \frac{\Omega}{2\pi\phi}, \tag{3.4}$$

where v_i is the optical lattice velocity and other parameters are as described before.

They move with this velocity until they collide with one of the barriers, and are reflected with a velocity, v_r, expressed by

$$v_r = \sqrt{\frac{Ak_b}{2m} + (\omega \times 0.62 \times x_b)^2}, \tag{3.5}$$

where,

A = Potential amplitude

k_b= Boltzmann constant

m = Mass of Rb atom

ω = Angular trapping frequency in the x direction

x_b = Distance of the barrier from the centre of the trap,

and $v_r > v_i$.

3.4.1 Lattice velocity, v_i

In the slow lattice velocity regime, Fermi acceleration has little dependence on v_i, which means the velocity of the reflected atoms is effectively independent of the frequency of the potential, and the wavenumber of the potential. This is the case for the parameters used in this experiment. For higher lattice velocities, it is expected that v_r will depend more strongly on v_i. It was not experimentally necessary to look at a large v_i regime in order to observe the Fermi acceleration of atoms, but is something that could be investigated, and may provide interesting results in the future.

3.4.2 Reflection velocity, v_r

The reflection velocity, v_r, is the more important velocity to consider for Fermi acceleration since it is the velocity the particles are reflected from the barrier with, which is what makes the effect observed analogous to Fermi acceleration. An additional factor is included in Eq. 3.5 because the trap is not perfectly parabolic and flattens out towards the edges. For a value of $x_b = 50 \times 10^{-6}$ m, the factor by which the edges are shortened is equal to 0.62, hence the origin of this factor in the equation.
The reflection velocity and therefore the energy gained from Fermi acceleration, depends only on the height of the optical lattice amplitude, A, and the trapping frequency in the x direction (as long as v_i is small), as seen in Eq. 3.5.

3.5 Image Processing and Gaussian Fitting for Data Analysis

In this section, I will briefly describe the method used to analyse the images taken in the experiment, to both visually track the movement of the atom cloud and also to obtain physical values for v_i and v_r.

The first step of the data analysis was to create a visual image of the movement of the atom cloud over time. To do this the images taken in a sequence are processed, by loading the images and extracted the specific regions of interest and then normalising the data to enhance the quality. The regions of interest from each image across the sequence are put together to produce colour maps, like the ones displayed in figures 3.3, 3.4 and 3.5, where data can be visualised and the movement of the cloud of atoms is observed as it hits the barrier and reflects.

The second step was to isolate a method for calculating v_i and v_r. Comparing the experimental velocities of the atoms with the theoretical values is necessary to draw comparisons between the experiment and Fermi acceleration. The method involved fitting a Gaussian and tracking the maximum value of it for each image in a sequence. In order to execute this, the normalised data from the colour map has a Gaussian fit to it and the fitted parameters are printed. This is repeated for each image in a sequence and then the maximum values are plotted on a separate graph against time. v_i is found from the gradient during the times at which the cloud is moving towards the barrier and v_r is found from the

gradient at the times when the cloud is reflecting. It is important to note that, as previously mentioned, sometimes the cloud of atoms splits into two. When this happens, both clouds can be tracked and two Gaussian's can be plotted, however this is not essential and following the movement of one cloud is enough to to find the required velocity.

An example of how the Gaussian method is used is depicted in figure 3.6. This dataset was acquired at an amplitude of $5.77 \times 10^{-7} K$. A 2 ms slice of the color map from 6 to 8 ms, corresponding to a single image captured in the sequence, is selected. In this instance, two Gaussian functions are fitted to this slice. The maximum values of the gaussians, along with other important parameters, are recorded. Table 3.3 presents the essential parameters obtained from this fitting process. Other parameters can be used to give information about the cloud, for example σ can give an insight into the distribution of velocities.

Table 3.3: Table of example Gaussian Parameters used to find information about the velocity of the cloud

Gaussian 1		Gaussian 2	
Parameter	Value	Parameter	Value
μ_1	56	μ_2	141
σ_1	24	σ_2	25
A_1	0.24	A_2	0.19

3.6 Results

Figures 3.8, 3.9, 3.10 and 3.11 present the main results from the experiment.

The data used to find the velocities for different values of Ω, ϕ and the trapping frequency is displayed in figures 3.3, 3.4 and 3.5. However for the amplitude a new set of data was collected, at $f_x = 28\ Hz$. Figure 3.7 shows the colour maps of the data, showing the cloud of atoms moving and reflecting with the barrier. These images were taken from 0-50 ms in steps of 2 ms.

Figures 3.8 and 3.9 displays the results for Ω and ϕ respectively. The black line represents v_r and for both parameters does not vary heavily despite the changing in Ω or ϕ, which agrees with the theory.

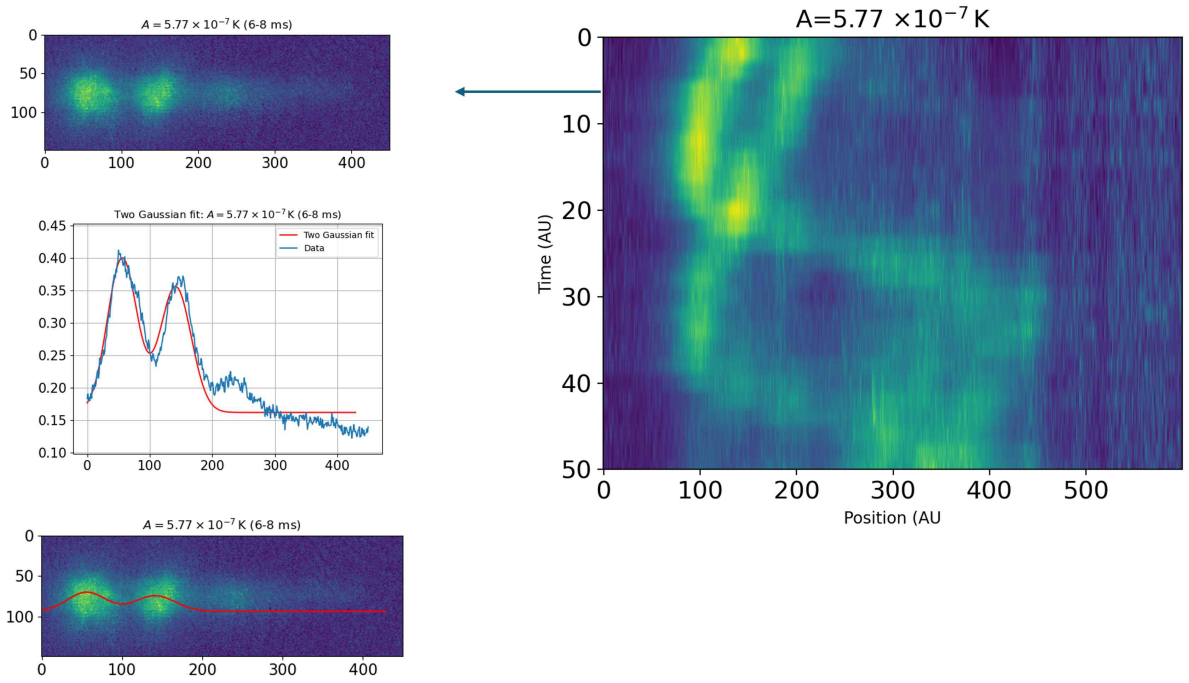

Figure 3.6: Example of the Gaussian fitting for data analysis where a slice of a colour map is taken, in this case at A = $5.77 \times 10^{-7} K$ and a Gaussian is fit to the cloud of atoms to obtain the maximum value

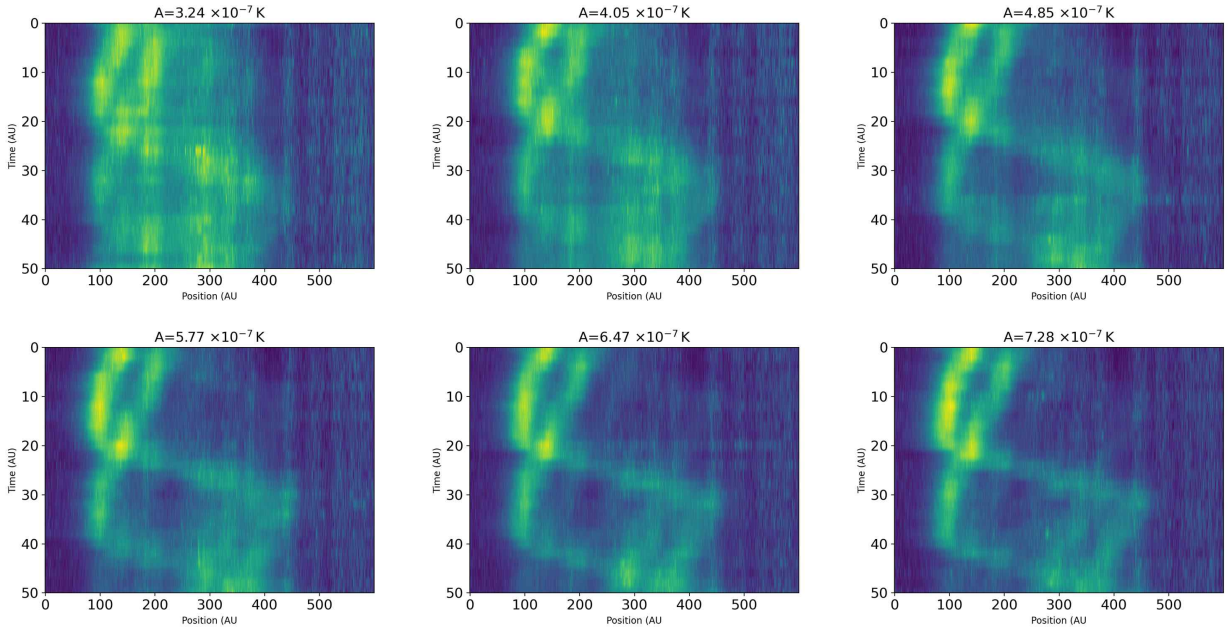

Figure 3.7: Integrated density profiles of a BEC under action of a one-dimensional periodic potential, at different values of A. The x axis displays the position of the atom cloud in pixels and the y axis is the time in ms. An image is taken every 2 ms from 0-50 ms.

On both graphs, the experimental v_i is plotted in red and the theoretical v_i is plotted in blue. In both cases the experimental and theoretical values match up nicely and follow the same pattern, showing

experimentally that the set-up displays the same behaviour of v_i for the atoms as the theory does.

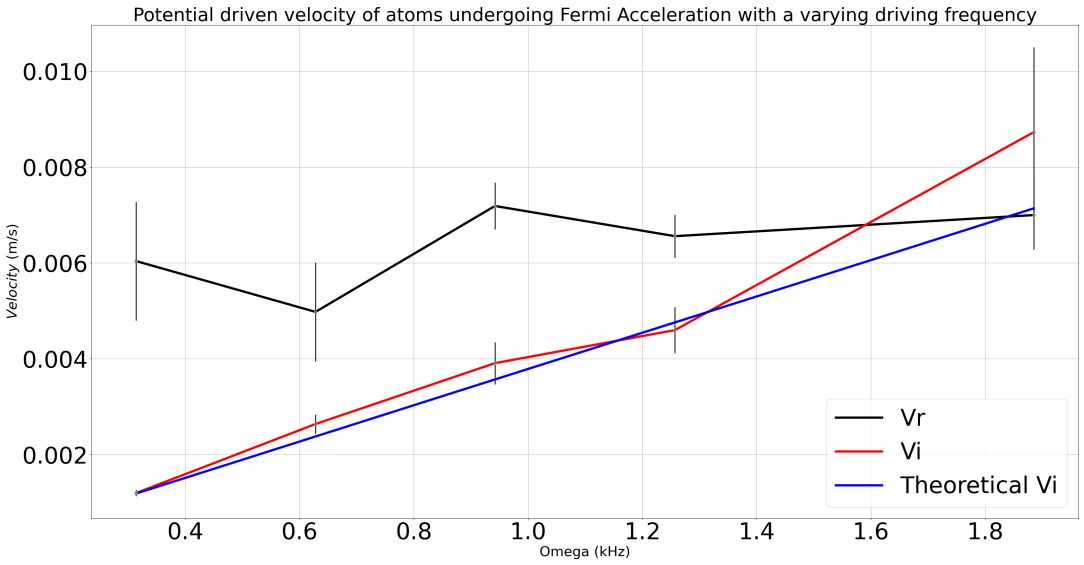

Figure 3.8: Graph displaying the theoretical optical latticed velocity, in blue, the experimental optical lattice velocity, red, and the experimental reflection velocity of atoms undergoing Fermi Acceleration at varying Ω values, from 0.3 to 2 kHz.

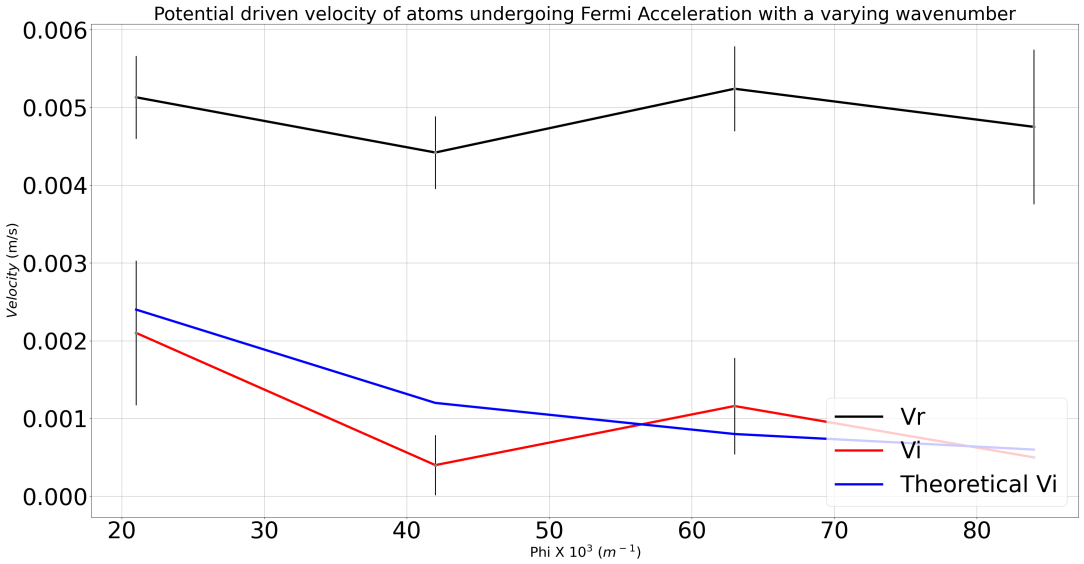

Figure 3.9: Graph displaying the theoretical optical latticed velocity, in blue, the experimental optical lattice velocity, red, and the experimental reflection velocity of atoms undergoing Fermi acceleration at varying ϕ values, from 20×10^3 to 90×10^3 m^{-1}

Figures 3.10 and 3.11 displays the results for A and the trapping frequency respectively. In both cases

a theory line with Eq. 3.5 has been plotted in red and v_r from experimental data has been plotted in black. The experimental data matches up very well with the theory which suggests the experiment is an effective system for modelling Fermi-Acceleration.

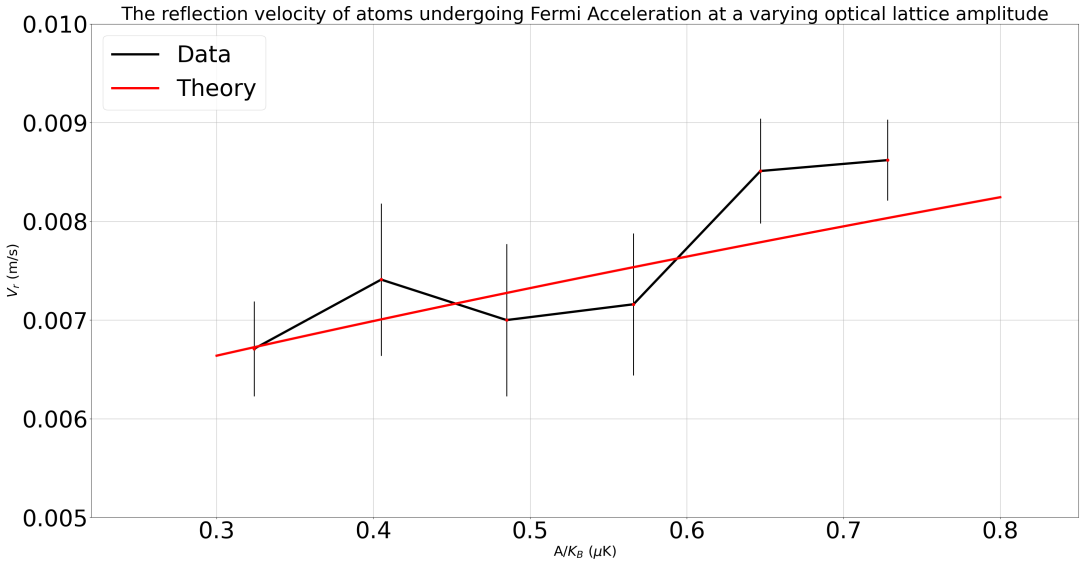

Figure 3.10: Graph displaying the theoretical reflection velocity in red and the experimental reflection velocity, in black, of atoms undergoing Fermi acceleration at a varying optical lattice amplitude.

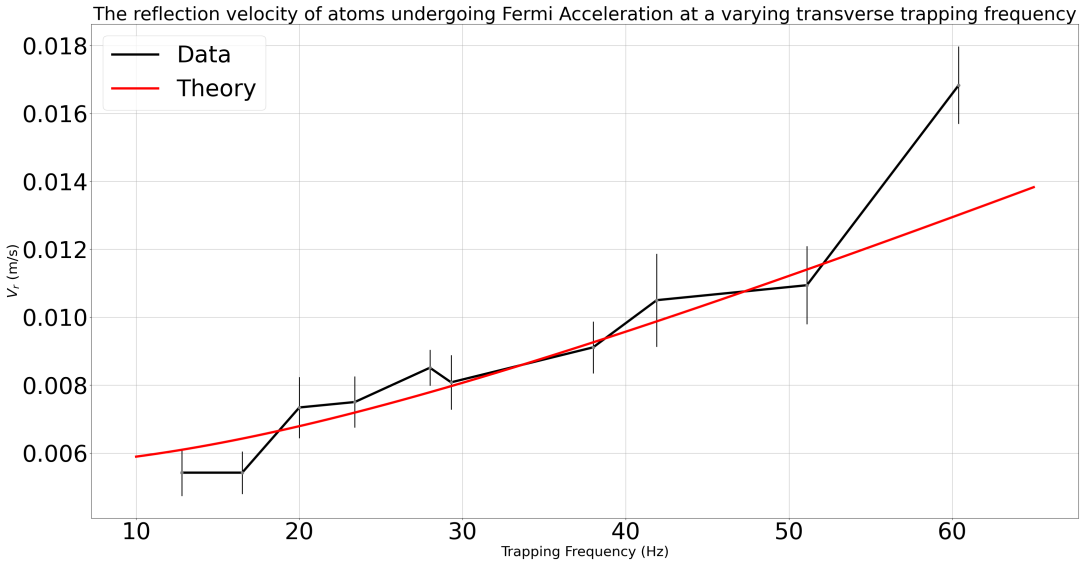

Figure 3.11: Graph displaying the theoretical reflection velocity, in red and the experimental reflection velocity, in black, of atoms undergoing Fermi acceleration at a varying trapping frequency.

Chapter 4

Discussion and future work

4.1 Extension of Fermi Acceleration

Bell's power law distribution links the spectrum of the accelerated atoms to the atom losses that occur during Fermi Acceleration, [48]. This law is at the foundation of diffusive shock acceleration, but has never been experimentally verified before. For this to be verified experimentally, a similar experiment, as discussed in the previous section, can be carried out. In this experiment the barrier thickness can be changed and the effect this has on the number of atoms as well as the width of the velocity distribution of the reflected atoms, is observed. It is expected that at thinner barriers there would be more losses of atoms and at thicker barriers less losses. Another possible extension would be to possibly look outside of the small v_i regime and consider what changes would be made to v_r when the optical lattice velocity also effects the final velocity.

4.2 Fountain Effect

Some preliminary work was carried out on the superfluid fountain effect, specifically assessing how viable it would be to demonstrate the effect using the experimental set-up.

Superfluidity was experimentally discovered as a property of helium II in 1938 by Allen and Misener [54]. One of the more unusual effects relating to the superfluidity of Helium II was the discovery of

the fountain effect. The effect can be observed when liquid helium II is split into two with a capillary between the two parts. When one side is heated, a jet of the liquid Helium II is produced as a result. The effect has been simulated numerically in a BEC [55] but is yet to be experimentally shown and would provide some key experimental evidence for the superfluidity of a BEC.

To assess the viability, the cloud of atoms was separated into two pieces by an optically induced barrier, which was displayed onto the atoms by the DMD. The idea is for one side of the barrier to be heated before a small channel is introduced between the two halves (capillary). Predicted behaviour based on the simulations and the behaviour in helium II suggest that for the system to achieve thermodynamic equilibrium, atoms would flow from the cold to the hot side of the barrier. This is because a superfluid cannot transport heat or entropy so the temperature gradient can only be decreased by adding zero-entropy cold atoms to the heated side.

From the preliminary work carried out it is has been concluded that it is very easy to split the cloud into two halves in trap. This is done by elongating the cloud of atoms in the dipole trap and then introducing the optical induced barrier. However, viewing the two halves separately in time of flight (TOF) has been challenging since the two halves tend to overlap as they expand. This was overcome by the addition of a kicking potential, with the DMD, which forced the two halves to pass through each other and therefore separate. Figure 4.1 shows the image of the split cloud in TOF with and without the kick. Introducing the kick resulted in a huge loss in atoms, means that the experiment requires a large BEC, of around 100k atoms, at the start. The loss in atom number was also a challenge for finding a method to heat one side of the cloud. To date a suitable method that has a good signal and a workable number of atoms, has not been found. Another issue that has not been resolved is finding the required width of the capillary. This length needs to be small enough so that the only atoms able to move between the two sides are from the zero-viscosity superfluid component. In the future, if these issues are resolved, then the system should be capable of giving a clear demonstration of the effect.

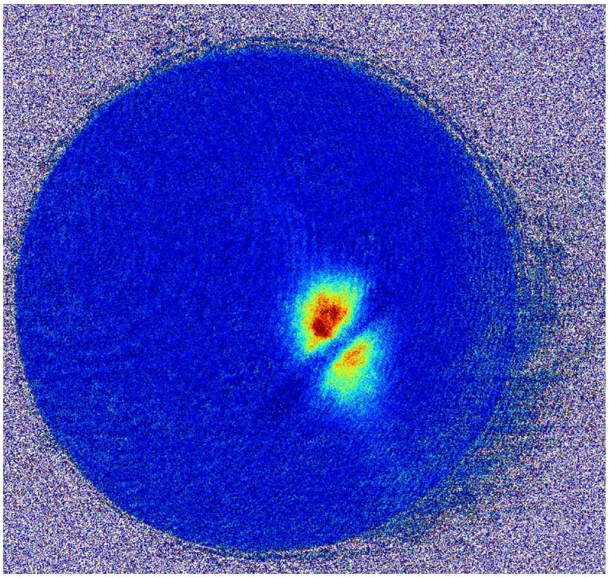

A) WITHOUT KICK

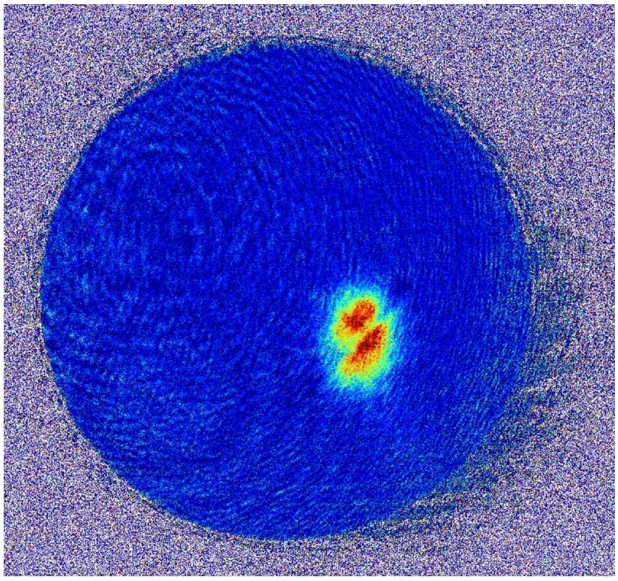

A) WITH KICK

Figure 4.1: The images show the cloud of atoms split by a 151 pixel barrier with and without the kick in time of flight. Both images show a clear split of the atoms into two halves and both halves appear to contain roughly equal amounts of atoms

4.3 Andreev-Bashkin Effect

The Andreev-Bashkin effect is an effect experienced by a superfluid. A superfluid has zero viscosity and causes zero drag effect on a non-superfluid (normal fluid). It has been predicted in papers that there may be a dispersion free drag effect between separate superfluid materials known as the Andreev-Bashkin effect, [56].

In the experimental set-up it could be possible to observe the Andreev-Bashkin effect take place between vortices. This could be done by creating spinor BECs, which can be considered as a collection of three separate BECs- one for each component of the magnetic Zeeman state. By performing Stern-Gerlach pulses on the three components, they can be spatially separated. A Stern Gerlach pulse can be created by letting the atoms free-fall while applying a magnetic field gradient on them. Once the components are separated, it is possible to imprint quantised vortices onto two or more of the components and then recombine them using reverse Stern-Gerlach pulses. If any interaction between the imprinting vortex components were observed, this would be strong evidence for the Andreev-Bashkin effect being seen in a BEC and would further add to the evidence a BEC

behaves as superfluid.

The Andreev Baskin effect is often discussed in relation to neutron star models [57] since the centre of a neutron star is believed to be made of Bose Einstein condensates, [58] so could also be useful in the understanding of neutron stars as well.

Chapter 5

Conclusion

In summary, the experimental investigation has effectively demonstrated that cold atom experiments are a feasible set-up for modelling Fermi acceleration. Using a DMD, Fermi acceleration was simulated on a cloud of ultra-cold atoms by generating an optical potential which drove the atoms towards a barrier where, upon collision, they reflected: an effect analogous to Fermi acceleration whereby particles interact with a shock wave. By observing the effects of changing the driving frequency (ω), wavenumber (ϕ), amplitude (A) and trapping frequency of the potential, allowed for the analysis of the effect changing these parameters had on both the optical lattice velocity (v_i) and the reflection velocity (v_r) of the cloud of atoms. The experimental results followed the theoretical predictions closely which demonstrates the validity of the experimental set-up for modelling Fermi acceleration. The success in modelling the effect suggests promising future developments in observing Fermi accceleration experimentally, such as to experimentally verify the Bell's power Law distribution, which has not been experimentally verified to date. The results also highlight the importance of cold atom experiments as a versatile tool for exploring wider physics phenomena.

Chapter 6

References

[1] Arthur L. Robinson. “Sodium Atoms Trapped With Laser Light”. *Science* 233, pp. 623–623. DOI: 10.1126/science.233.4764.623.a.

[2] E. L. Raab et al. “Trapping of Neutral Sodium Atoms with Radiation Pressure”. *Phys. Rev. Lett.* 59, pp. 2631–2634. DOI: 10.1103/PhysRevLett.59.2631.

[3] Nicolas Schlosser et al. “Sub-Poissonian loading of single atoms in a microscopic dipole trap”. *Nature* 411, pp. 1024–7. DOI: 10.1038/35082512.

[4] Timothy P. Softley. “Cold and ultracold molecules in the twenties”. *Proceedings of the Royal Society of London Series A* 479, p. 20220806. DOI: 10.1098/rspa.2022.0806.

[5] Bo Zhao and Jian-Wei Pan. “Quantum control of reactions and collisions at ultralow temperatures”. *Chem. Soc. Rev.* 51, pp. 1685–1701. DOI: 10.1039/D1CS01040A.

[6] Vivien Zapf, Marcelo Jaime, and C. D. Batista. “Bose-Einstein condensation in quantum magnets”. *Rev. Mod. Phys.* 86, pp. 563–614. DOI: 10.1103/RevModPhys.86.563.

[7] S. Pilati and M. Troyer. “Bosonic Superfluid-Insulator Transition in Continuous Space”. *Physical Review Letters* 108. DOI: 10.1103/physrevlett.108.155301.

[8] S. N. Bose. “Plancks Gesetz und Lichtquantenhypothese”. *Zeitschrift für Physik.* 26, pp. 178–181. DOI: 10.1007/BF01327326.S2CID186235974.

[9] Albert Einstein. “Quantentheorie des einatomigen idealen Gases”. *Königliche Preußische Akademie der Wissenschaften.*

[10] M.H. Anderson et al. “Observation of bose-einstein condensation in a dilute atomic vapor”. In: Jan. 2008, pp. 453–456. DOI: 10.1142/9789812813787_0062. URL: https://www.science.org/doi/10.1126/science.269.5221.198.

[11] K. B. Davis et al. “Bose-Einstein Condensation in a Gas of Sodium Atoms”. *Phys. Rev. Lett.* 75, pp. 3969–3973. DOI: 10.1103/PhysRevLett.75.3969.

[12] C. C. Bradley et al. “Evidence of Bose-Einstein Condensation in an Atomic Gas with Attractive Interactions”. *Phys. Rev. Lett.* 75, pp. 1687–1690. DOI: 10.1103/PhysRevLett.75.1687.

[13] I. M. Georgescu, S. Ashhab, and Franco Nori. “Quantum simulation”. *Rev. Mod. Phys.* 86, pp. 153–185. DOI: 10.1103/RevModPhys.86.153.

[14] Andrew D. Ludlow et al. “Optical atomic clocks”. *Rev. Mod. Phys.* 87, pp. 637–701. DOI: 10.1103/RevModPhys.87.637.

[15] Boyuan Wang. “Review on Bose-Einstein Condensation”. *Highlights in Science, Engineering and Technology* 38, pp. 19–29. DOI: 10.54097/hset.v38i.5689.

[16] Silvana Palacios Alvarez et al. “Single-domain Bose condensate magnetometer achieves energy resolution per bandwidth below $\hbar$”. *Proceedings of the National Academy of Sciences* 119, e2115339119. DOI: 10.1073/pnas.2115339119.

[17] S. Wildermuth et al. “Sensing electric and magnetic fields with Bose-Einstein condensates”. *Applied Physics Letters* 88, p. 264103. DOI: 10.1063/1.2216932.

[18] Lan Xu et al. “Non-Markovian enhanced temperature sensing in a dipolar Bose-Einstein condensate”. *Phys. Rev. A* 108, p. 022608. DOI: 10.1103/PhysRevA.108.022608.

[19] H. Müntinga et al. “Interferometry with Bose-Einstein Condensates in Microgravity”. *Phys. Rev. Lett.* 110, p. 093602. DOI: 10.1103/PhysRevLett.110.093602.

[20] Stephen Thomas et al. “Modeling Atom Interferometry Experiments with Bose-Einstein Condensates in Power-Law Potentials”. *Atoms* 10. DOI: 10.3390/atoms10010034.

[21] Zhe Luo, E. R. Moan, and C. A. Sackett. “Semiclassical Phase Analysis for a Trapped-Atom Sagnac Interferometer”. *Atoms* 9. DOI: 10.3390/atoms9020021.

[22] Daniel Gochnauer et al. “Interferometry in an Atomic Fountain with Ytterbium Bose–Einstein Condensates”. *Atoms* 9. DOI: 10.3390/atoms9030058.

[23] Remi Geiger et al. “High-accuracy inertial measurements with cold-atom sensors”. *AVS Quantum Science* 2, p. 024702. DOI: 10.1116/5.0009093.

[24] F. Riehle et al. “Optical Ramsey spectroscopy in a rotating frame: Sagnac effect in a matter-wave interferometer”. *Phys. Rev. Lett.* 67, pp. 177–180. DOI: 10.1103/PhysRevLett.67.177.

[25] Franco Dalfovo et al. “Theory of Bose-Einstein condensation in trapped gases”. *Rev. Mod. Phys.* 71, pp. 463–512. DOI: 10.1103/RevModPhys.71.463.

[26] D. H. J. O’Dell and C. Eberlein. “Vortex in a trapped Bose-Einstein condensate with dipole-dipole interactions”. *Phys. Rev. A* 75, p. 013604. DOI: 10.1103/PhysRevA.75.013604.

[27] A. Gallemí et al. “Quantized vortices in dipolar supersolid Bose-Einstein-condensed gases”. *Phys. Rev. A* 102, p. 023322. DOI: 10.1103/PhysRevA.102.023322.

[28] E.P. Gross. “Structure of a quantized vortex in boson systems”. *Il Nuovo Cimento* 20, pp. 454–477. DOI: 10.1007/BF02731494.

[29] L. P. Pitaevskii. “Vortex Lines in an Imperfect Bose Gas.” *Journal of Experimental and Theoretical Physic* 13, pp. 451–454.

[30] Toshiya Kinoshita, Trevor Wenger, and David S. Weiss. “All-optical Bose-Einstein condensation using a compressible crossed dipole trap”. *Phys. Rev. A* 71, p. 011602. DOI: 10.1103/PhysRevA.71.011602.

[31] Helmut Ritsch et al. “Cold atoms in cavity-generated dynamical optical potentials”. *Reviews of Modern Physics* 85, pp. 553–601. DOI: 10.1103/revmodphys.85.553.

[32] Ray Fulton et al. “Controlling the motion of cold molecules with deep periodic optical potentials”. *Nature Physics* 2, pp. 465–468.

[33] Rudolf Grimm, Matthias Weidemüller, and Yuri Ovchinnikov. "Optical Dipole Traps for Neutral Atoms". *Advances in Atomic, Molecular, and Optical Physics* 42, p. 95. DOI: 10.1016/S1049-250X(08)60186-X.

[34] Cecilia Muldoon et al. "Control and manipulation of cold atoms in optical tweezers". *New Journal of Physics* 14, p. 073051. DOI: 10.1088/1367-2630/14/7/073051.

[35] Y. Wang et al. "Preparation of hundreds of microscopic atomic ensembles in optical tweezer arrays". *npj Quantum Inf* 6, p. 54.

[36] R.V. Brooks et al. "Preparation of one 87Rb and one 133Cs atom in a single optical tweezer". *New Journal of Physics* 23. DOI: 10.1088/1367-2630/ac0000.

[37] Rudolf Grimm, Matthias Weidemüller, and Yurii B. Ovchinnikov. "Optical Dipole Traps for Neutral Atoms". URL: https://www.sciencedirect.com/science/article/pii/S1049250X0860186X, pp. 95–170. DOI: https://doi.org/10.1016/S1049-250X(08)60186-X.

[38] Zhao Chen et al. "Blue-detuned optical atom trapping in a compact plasmonic structure". *Photon. Res.* 5, pp. 436–440. DOI: 10.1364/PRJ.5.000436.

[39] Jiandong Bai et al. "Towards implementation of a magic optical-dipole trap for confining ground-state and Rydberg-state cesium cold atoms". *Journal of Physics B: Atomic, Molecular and Optical Physics* 53, p. 155302. DOI: 10.1088/1361-6455/ab91de.

[40] Daniel Benedicto Orenes. "Realization of a spin-1 Bose-Einstein condensation experiment". URL: http://etheses.bham.ac.uk/id/eprint/8073.

[41] M. Egorov et al. "Measurement of s-wave scattering lengths in a two-component Bose-Einstein condensate". *Phys. Rev. A* 87, p. 053614. DOI: 10.1103/PhysRevA.87.053614.

[42] Daniel A. Steck. "Alkali D Line Data". URL: https://steck.us/alkalidata/.

[43] "What Is the Definition of a TTL (Transistor-Transistor Logic) Compatible Signal". URL: https://knowledge.ni.com/KnowledgeArticleDetails?id=kA03q000000YRMRCA4&l=en-US.

[44] John D. Jackson. "Visual Analysis of a Texas Instruments Digital Micromirror Device". URL: http://www2.optics.rochester.edu/workgroups/cml/opt307/spr05/john/.

[45] Tian-You Gao et al. “Observation of Atomic Dynamic Behaviors in the Evaporative Cooling by In-Situ Imaging the Plugged Hole of Ultracold Atoms”. *Chinese Physics Letters* 35, p. 086701. DOI: 10.1088/0256-307x/35/8/086701.

[46] Aviv Keshet; Wolfgang Ketterle. “A distributed, graphical user interface based, computer control system for atomic physics experiments”. *Rev. Sci. Instrum.* DOI: https://doi.org/10.1063/1.4773536.

[47] ENRICO Fermi. “On the Origin of the Cosmic Radiation”. *Phys. Rev.* 75, pp. 1169–1174. DOI: 10.1103/PhysRev.75.1169.

[48] A.R. Bell. “The acceleration of cosmic rays in shock fronts - I.” *mnras* 182, pp. 147–156. DOI: 10.1093/mnras/182.2.147.

[49] G.F. Krymskii. “A regular mechanism for the acceleration of charged particles on the front of a shock wave”. *Akademiia Nauk SSSR Doklady* 234, pp. 1306–1308.

[50] R.A. Chevalier. “Cosmic Ray Acceleration in Supernova Remnants”. In: *International Cosmic Ray Conference*. Vol. 10. International Cosmic Ray Conference. Jan. 1977, p. 67. URL: https://ui.adsabs.harvard.edu/abs/1977ICRC...10...67C.

[51] Haihong Che and Gary Zank. “A Brief Review on Particle Acceleration in Multi-island Magnetic Reconnection”. *Journal of Physics: Conference Series* 1332, p. 012003. DOI: 10.1088/1742-6596/1332/1/012003.

[52] Arto Sandroos, Gang Li, and Lulu Zhao. *First and Second-order Fermi Acceleration at Parallel Shocks*. 2014. arXiv: 1408.3022 [physics.space-ph]. URL: https://arxiv.org/abs/1408.3022.

[53] M Bustamante and et al Carrillo Montoya. “High-energy cosmic-acceleration”. URL: https://cds.cern.ch/record/1249755. DOI: 10.5170/CERN-2010-001.533.

[54] J. F. ALLEN and H. JONES. “New Phenomena Connected with Heat Flow in Helium II”. URL: https://doi.org/10.1038/141243a0, pp. 243–244. DOI: 10.1038/141243a0..

[55] Tomasz Karpiuk et al. “Superfluid fountain effect in a Bose-Einstein condensate”. *Phys. Rev. A* 86, p. 033619. DOI: 10.1103/PhysRevA.86.033619.

[56] A.F. Andreev and E.P. Bashkin. “Three-velocity hydrodynamics of superfluid solutions”. *Soviet Journal of Experimental and Theoretical Physics* 42, p. 164.

[57] S. I. Shevchenko and D. V. Fil. “The Andreev-Bashkin effect in a two-component Bose gas”. *Journal of Experimental and Theoretical Physics* . DOI: 10.1134/s106377610707028x.

[58] C. Pethick, Thomas Schaefer, and A. Schwenk. “Bose-Einstein condensates in neutron stars”. *arXiv preprint arXiv:1507.05839* .